MULTI-DIMENSIONAL FIBER OPTIC SENSORS FOR BIOMEDICAL AND SOFT ROBOTIC APPLICATIONS

by

LI XU

(Under the Direction of Mable P. Fok)

ABSTRACT

Optical fiber sensing has been widely used in in biomedical and soft robotics applications due to the unique features such as small size, high sensitivity, flexibility, and immunity to electromagnetic interference. Among various types of optical fiber sensors, fiber Bragg grating (FBG) sensor has drawn lot of attention due to its unique advantages such as compact size, simple fabrication process, and high sensitivity for various physical phenomenon.

In this thesis, several unique designs of FBG based sensors for biomedical and soft robotics applications are presented to achieve multi-dimensional measurement. FBG based sensors with different structures are used for sensing various physical parameters including contact force, bending curvature, and shape. Furthermore, a new interrogation scheme for FBG sensor is presented to simplify the measurement process of FBG as well as to enable real time sensing.

INDEX WORDS: Optical fiber sensor, fiber Bragg grating, biomedical sensing, soft robotics.

MULTI-DIMENSIONAL FIBER OPTIC SENSORS FOR BIOMEDICAL AND SOFT ROBOTIC APPLICATIONS

by

LI XU

B.Eng., Shandong University, China, 2010

A Thesis Submitted to the Graduate Faculty of The University of Georgia in Partial Fulfillment of the Requirements for the Degree

MASTER OF SCIENCE

ATHENS, GEORGIA

2017

MULTI-DIMENSIONAL FIBER OPTIC SENSORS FOR BIOMEDICAL AND SOFT ROBOTIC APPLICATIONS

by

LI XU

Major Professor: Mable P. Fok

Committee: Peter A. Kner
Xianqiao Wang

Electronic Version Approved:

Suzanne Barbour
Dean of the Graduate School
The University of Georgia
December 2017

ACKNOWLEDGEMENTS

First, I would like to thank my supervisor Dr. Mable Fok for providing the great opportunity joining the lab and generous help to my Master study. I really enjoy the wonderful research environment in this lab. I am also grateful to the graduate students, Jia Ge, Ruizhe Lin, Qidi Liu, Mei Yang and Ning Liu for their kindly assistance in both research and life giving me motivation to finalize my program and thesis during more than two years' study. Furthermore, thanks all the hard working undergraduate students, Alex, Aneek, Jay, Luis and Phiet who supported my work and helped me with experiment.

I would also like to thank Dr. Kner and Dr. Wang for participating in my graduation committee and helping to improve my research work, and thank all staffs and colleges in Engineering helping with all the trifles and graduation.

Lastly, thank my parents for offering the most important encouragement through phone calls from distant China. They supported my decision to study abroad and encouraged me to overcome hard times during the last two years. I can not imagine finishing my thesis without their unconditional love and encouragement.

TABLE OF CONTENTS

Page

LIST OF FIGURES

Page

CHAPTER 1

INTRODUCTION

During the past two decades, fiber optic sensing technology has been intensively developed and widely applied in various of fields due to the fast growth of optical communications industries and the mature fabrication process of different types of optical fiber. Instead of being used as the data transmission medium in optical communications, optical fiber can also be used as the sensing element to detect the changes in surrounding environment. The transmitted light is sensitive to the physical parameters around the fiber, such as applied force, strain, pressure, temperature, or any disturbances that change the physical property of optical fiber. By monitoring the changes of the transmitted or reflected light in a proper design, corresponding measurement of one or multiple physical parameters around the fiber can be achieved.

The unique features of optical fiber, such as small size, light-weight, low-cost, high sensitivity, fast data transmission speed, long measurement distance, and immunity to electromagnetic interference, making it a promising and advanced solution for many sensing applications [1,2]. The diameter of a typical single mode optical fiber is only 125 um, which is extremely small compared to electrical wires and components, making it possible for small-scale applications with multiple sensing points. Since optical fiber is usually made of glass and light is used to carry the sensing information, fiber optic sensors are usually resisting to harsh and extreme environment such as high voltage, high temperature, high humidity, corrosive, and electro-magnetic environments, where conventional electronics based sensors have limited performance.

In addition, since optical fibers are designed for high-speed and long-distance data transmission in optical communications, a single fiber can serve both sensing and data transmitting. Thus, optical fiber sensors are essential real-time sensors with short response time, and are also good for remote sensing in a longer sensing distance. Due to these unique advantages over conventional sensors, optical fiber sensor is becoming promising candidate for a variety of applications, especially in biomedical and soft robotics applications.

Sensor plays an important role in biomedical engineering to detect all kinds of information for medicine, biology, healthcare and safety purposes. Nowadays soft robots are becoming increasing popular for biomedical treatment procedures, which are often inspired from biological systems and consist of soft materials similar to those in living organisms. Compared to conventional robots, soft robots have advantages such as safe human-machine interaction and adaptability to wearable devices. At the meanwhile, they have higher requirements such as flexibility, small size and extensibility for sensors. Real-time monitoring of the soft robots during a biomedical treatment procedure is extremely important, contact force, pressure and movement monitoring are usually necessary for safe operation. In recent decades, sensors for biomedical applications and soft robotics are widely studied, electrical sensors are widely used in these areas. However, these conventional electronics based sensors have limitations such as bulky system and can be easily interfered by electromagnetic signals. For biomedical applications under magnetic resonance imaging (MRI) environment or soft robots with compact and flexible structures, electrical sensors usually have limited performance. Compared to electrical sensors, the unique properties of fiber optic sensor make it a perfect candidate for both biomedical and soft robotic applications.

There are mainly four categories of fiber optic sensors [3-5], including intensity-based sensors, wavelength-varying sensors, polarization-modulating sensors and phase-modulating sensors. Intensity-based sensors detect the changes in light intensity and correlate intensity variation to change in external factors such as temperature and force. In this method, a movable reflector or a cavity is needed for pressure, strain and distance sensing by inducing light intensity change during reflection in the cavity. Wavelength-varying sensors map changes in wavelength or frequency to external parameters such as strain and temperature. By measuring the wavelength shift of a particular in-line structure, the change of external parameters can be quantitatively analyzed. Fiber Bragg grating (FBG) is one of the wavelength-varying sensors. Polarization-modulating sensors usually measure the rotations of the polarization states caused by Faraday effect to detect magnetic fields or voltages. Phase-modulating sensors are based on two beam interferometer or multi-beam interferometer. The interferometer used for sensors can be constructed by Michelson interferometer, Mach-Zehnder interferometer, Fabry-Perot interferometer and Ring interferometer. External pressure and force can be detected through these interference based methods.

Among these various types of fiber optic sensors, FBG based sensor stands out from the rest. Compared to other sensing schemes, FBG has relative low complexity, wide applicability, small size, low cost, mature fabrication process, and easy for multiplexing. In this thesis, we mainly focus on the use of FBG based sensors for contact force measurement in biomedical catheters as well as curvature and shape measurement of irregular and flexible objects. The physical structure of FBG and sensing principle of FBG based sensors are first introduced in Chapter 2. Then we develop several FBG based contact force sensing approaches for mono-directional steerable catheter, bi-directional steerable catheters and non-steerable catheters, as introduced in Chapter 3.

Standard FBG, FBG pair and spirally mounted FBG are embedded with the steerable catheters for contact force measurement, temperature insensitive performance or temperature compensating method are demonstrated. In Chapter 4, FBG based soft sensors for multi-dimensional curve sensing and shape measurement in soft robotics applications are developed. Bending curvatures and 3D shape of test objects are successfully measured. Furthermore, a soft stretchable sensor which is capable of measuring multiple parameters is developed. Strain, torsion direction, and bending curvature can be measured through the use of an off-center embedded FBG. Conclusions and future work are discussed in Chapter 5 [6-9].

CHAPTER 2

FIBER BRAGG GRATING BASED FIBER OPTIC SENSORS

2.1 Introduction

FBG is a fiber optic in-line structure, it is written inside an optical fiber by constructing a large number of high refractive index Bragg reflectors (gratings) within a short segment of optical fiber [10]. The first FBG was reported by Hill et al. in 1978, since then it has been well studied and widely used in a wide range of applications including optical communications, sensing, and signal processing. Based on its working principle, FBG can be used for sensing directly by measuring the wavelength change of the Bragg wavelength. The grating structure is sensitive to the physical changes in the surround environment of the optical fiber, thus, these changes can be correlated to the reflection wavelength of the FBG. This makes FBG capable of measuring a wide range of parameters, including force, strain, pressure, temperature, etc., which are commonly desired parameters in a number of fields. In general, the gratings are directly written in the core area of an optical fiber. This makes FBG based sensor relatively simple, without any complex structures as found in the polarization or interference based sensors. In addition, FBG based sensor has the capability for easy multiplexing, that multiple FBGs (with same or different center wavelengths) can be written along a single piece of optical fiber, which is good for multi-points, multi-function, and remote sensing. Due to these features, among different types of optical fiber sensing techniques, FBG based sensor is the most widely used technology in sensing applications [11].

FBG can be fabricated mainly in two ways [12], the first one is based on two-beam interference method. In this method, two overlapping ultraviolet (UV) light beams are made to interfere to produce an interference pattern with different light intensity. A photosensitive optical fiber is usually used to write the gratings. The refractive index of the photosensitive fiber changes according to the intensity of light that it is exposed to. With the interference pattern, periodical grating structure with specific period can be obtained. The second method is phase mask based method. A phase mask is used as a diffractive optical element made by etching grating patterns on fused silica substrates, UV light incidents normally to the phase mask and passes through, and is diffracted by the periodic corrugations, creating an interference pattern [13]. Then corresponding gratings can be written on to the photosensitive fiber. The fabrication process of FBG is relative simple and becomes very mature nowadays, as a result, the fabrication cost of a standard FBG is very low, which makes FBG a favored solution and becoming increasingly useful [14].

2.2 Mathematical Model of Fiber Bragg Gratings

FBG is a type of in-line distributed Bragg reflector constructed in a short segment inside the core area of a single mode optical fiber, usually within 5 mm to 2 cm. The refractive index of the gratings (n_g) are higher than the fiber core (n_c), as shown in Figure 2.1. Thus, there is a periodically refractive index variation in the fiber core area. For a standard single mode fiber, the diameter of the core area is 8 μm, and the total diameter including the cladding area is 125 μm.

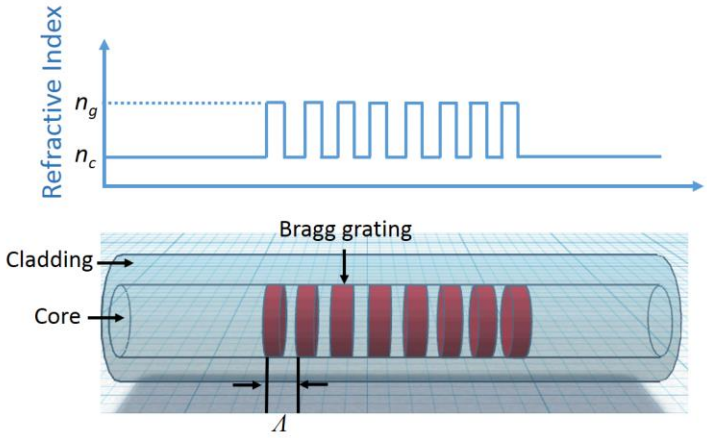

Figure 2.1. Schematic diagram of the fiber Bragg grating structure and the periodical refractive index variation.

The incident light will be reflected or refracted through the grating planes, such that different extends of interference occur at different wavelengths, resulting in either reflection or transmission of that wavelength. At each grating plane, part of the light is refracted through the grating while the other part is reflected backward. Since the reflected light from different gratings have path differences, different amounts of interference are resulted at different wavelengths – depending on the phase difference between each path. In the backward propagating light, constructive interference is resulted only if the path difference is the integer multiple of the wavelength (in-phase). The rest of light (out-of-phase) will be destructive interfered. In other words, when the wavelength satisfies the condition shown in Eq. (2.1) [15,16], light at this wavelength will be constructive interfered in the backward propagating direction and be reflected back to the input port:

$$\lambda_B = 2n\Lambda \tag{2.1}$$

where λ_B is the Bragg wavelength, n is the effective refractive index and Λ is the period of gratings. Light at other wavelengths will be transmitted through the FBG.

As mentioned in the introduction, the periodical grating structure is extremely sensitive to the surrounding environment. Strain along the FBG causes the Bragg grating wavelength shift because a change in strain changes the grating period (Λ). A positive strain (stretching) results in an increase in the Bragg wavelength, while a negative strain (compression) results in a decrease in the Bragg wavelength. In addition, the temperature changes cause thermal expansion along the fiber, and result in changes in the refractive index of the gratings and the optical fiber. The relationship between Bragg wavelength and the change in strain and temperature is described by Eq. (2.2),

$$\Delta\lambda_B = [(1 - p_e)\varepsilon + (\alpha_\Lambda + \alpha_n)\Delta T]\,\lambda_B \tag{2.2}$$

where p_e is the photo-elastic coefficient, α_Λ is the thermal expansion coefficient and α_n is the thermo-optic coefficient. Due to the relationship between the strain/temperature and the Bragg wavelength shift, strain and temperature are the two most commonly measured parameters of an FBG based sensor.

Previous study shows for a typical silica fiber, the wavelength-temperature sensitivities of an FBG sensor around 1550 nm is around 13 pm/^{o}C. The photo-elastic coefficient p_e is given by Eq. (2.3):

$$p_e = n^2/2[\rho_{12} - \nu(\rho_{11} - \rho_{12})] \tag{2.3}$$

where ρ_{11} and ρ_{12} are the components of fiber optic strain sensor and ν is the Poisson's ratio. For a silica fiber, the wavelength-strain sensitivities of an FBG sensor at 1550 nm has been measured to be around 1.15 pm/με [17].

It is worth mentioning that since FBG is sensitive to both the strain and temperature, this could become a significant limitation of FBG based sensors when both strain and temperature are changing at the same time. Usually, a reference grating in the same sensing environment can be

sued to distinguish effect caused by strain and temperature [24], and many designs can be implemented to build temperature insensitive sensors.

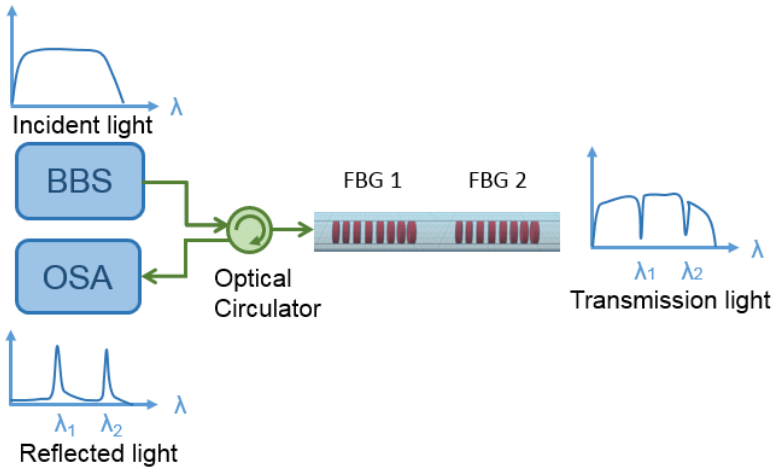

Figure 2.2. Test setup of FBG based sensing systems. BBS: optical broadband source; OSA: optical spectrum analyzer; FBG: fiber Bragg grating.

In a typical Bragg grating with an average refractive index n_0 of fiber core. The refractive index along the FBG can be expressed as

$$n(x) = n_0 + \Delta n \cos(\frac{2\pi x}{\Lambda}) \tag{2.4}$$

Where Δn is the amplitude of the induced refractive-index perturbation and x is the distance along the fiber. The reflectivity of a grating with constant modulation amplitude and period is expressed as

$$R(l,\lambda) = \frac{\Omega^2 \sinh^2(sl)}{\Delta k^2 \sinh^2(sl) + S^2 \cosh^2(sl)} \tag{2.5}$$

Where R(l,λ) is the reflectivity governed by grating length l and wavelength λ. Ω is the coupling coefficient, $\Delta k = k - \pi/\lambda$ is the detuning wave vector, $k = 2\pi n_0/\lambda$ is the propagation constant, $s = \sqrt{\Omega^2 - \Delta k^2}$, a general expression for the approximate full width at half-maximum bandwidth of a grating is as shown in following equation

$$\Delta\lambda = \lambda_B \alpha \sqrt{(\frac{\Delta n}{2n_0})^2 + (\frac{1}{N})^2} \tag{2.6}$$

Where N is the number of the gratings, α usually changes from 0.5 to about 1 when the reflection ratio increase to 100%.

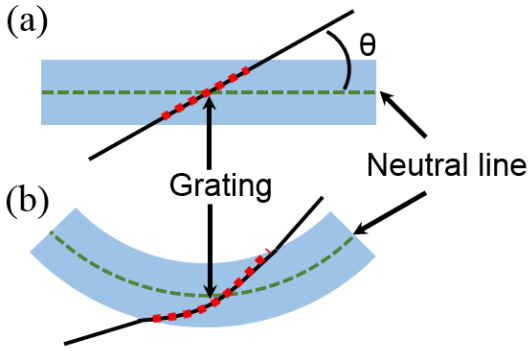

Figure 2.3. FBG based sensor for curvature measurement. (a) An FBG is embedded in a beam without any bending. (b) Deformation on FBG when the beam is bended.

If an FBG is embedded in a beam with a certain thickness as shown in Fig. 2.3, the strain gradient on the FBG caused by bending can be expressed by

$$\varepsilon(x) = k(2x - l)\sin(2\theta)/4 \tag{2.7}$$

Where l is the grating length, x is different point of the grating. K is the curvature of the neutral line and θ is the angle between FBG and neutral line as shown in Fig. 2.3. Then, the effective bandwidth of the grating can be expressed by

$$\Delta\lambda_{chirp} = \int_0^l \delta\lambda dx = \lambda_B kl(1 - P_e)\sin(2\theta)/2 \tag{2.8}$$

As shown in equation 2.8, when the bending curvature increase, the effective bandwidth of the chirped grating also increase. This feature can be used for curvature sensing in the following chapters.

Using these equations, the reflection spectral response of a uniform Bragg grating can be described. As the number of gratings (N) increase, the bandwidth will decrease, which means when

the grating period is fixed for a certain FBG, as the length of grating area increase, the reflection spectrum bandwidth decrease. The refraction index change usually uniform along the FBG, the value of the change is reduced when the grating length increase with a constant maximum grating reflectivity. The bandwidth of the gratings decreased with an increasing length of the gratings. And by increasing the grating length the FBG can construct a small bandwidths. However, the environment can cause difference in grating period resulting in out-of-phase periods leading to a broadening of Bragg grating. If the length of Bragg grating is fixed, the spectrum bandwidth decrease when the reflectivity the reflectivity decrease (Δn decrease).

Chirp in Bragg grating structure also changes the spectrum shape. A chirped FBG is a grating that has a varying grating period along the gratings. This can be achieved by varying either the grating period or the refractive index of the fiber core. As chirp value increase, the reflectivity response becomes broader and the reflection maximum decreases. These results are simulated and proved in some study [19].

To obtain the spectral information and the Bragg wavelength of the FBG, a test setup for FBG based sensors is shown in Figure 2.2. A broadband light source (BBS) is used as the light source, which provides light over a wide range of wavelength around the Bragg wavelength of the FBG. The BBS can be replaced with a tunable laser with fast wavelength sweeping range. An optical spectrum analyzer (OSA) is used to obtain the reflection or transmission spectrum of the FBG. Resolution of the OSA governs how accurate the change in Bragg wavelength can be measured. An optical circulator is used to launch the light source into the FBG and direct either the reflected light into the OSA for measurement. Optical spectra of the incident light, transmitted light and reflected light are illustrated in Figure 2.2, usually the transmitted light and the reflected light are complementary with each other. Furthermore, if two or more FBGs with different Bragg

wavelengths are connected in series, the reflected light from all the FBGs can be obtained through one measurement in the OSA. Multiple FBGs with different Bragg wavelength can be used at the same time by fusion splicing them together or writing them on the same fiber. This feature makes FBG based sensor suitable for multi-points sensing [18].

2.3 Applications of Fiber Bragg Grating for Sensing

Over the past two decades, different FBG based sensing schemes have been reported to achieve a variety of sensing functions. The most commonly used FBG based sensors are strain sensor and temperature sensor [20-21]. Based on the working principle, Bragg wavelength has a linear relationship with the applied strain and temperature. When the fiber is stretched or compressed, the deformation leads to a change in the grating period and then results in a shift of the Bragg wavelength. For FBG based temperature sensors, thermo-optic effect induces a variation of the refraction index of silica. Also, there is a contribution from thermal expansion effect which affect the grating period of FBG. FBG based strain and temperature sensors can be widely found in civil engineering applications where FBG based strain sensors are used for continuous lifetime health monitoring of bridges, dams, buildings and tunnels, and temperature sensors are used for lifetime monitoring of electricity facilities such as high voltage switch cabinets.

Besides strain and temperature measurement, FBG is also a good candidate for pressure sensing [22], chemical sensing [23] and accelerometer [24]. Usually, FBG based pressure sensors use structures like a cavity filled with flexible materials and deformable bases with an FBG embedded, the outside pressure can be transferred to the deformation of the FBG, then measured through Bragg wavelength shift. For FBG based chemical sensors, special chemical layers or metal layers are grown on a section of bare FBG, the chemical reactions in the surrounding solutions

will change the effective refractive index of the FBG. Thus, the characteristic of surrounding solutions such as the density and composition, can be detected by measuring the Bragg wavelength shift [25]. When FBG is used for building accelerometers, special structures such as a cantilever shelving or an axial compliant mechanism scroll compressor can be used with the FBG to transfer the acceleration to the stretch or compression on an FBG. In addition, due to its high tolerance to harsh environment, FBG based sensors are also widely used for temperature monitoring of high voltage switch cabinet, pressure monitoring in rocket fuel tanks, and long-term monitoring of the operating conditions of surface ship vertical launch system and missiles.

2.4 Interrogation methods for FBG based sensors

As shown in Fig. 2.2, using broadband light source and optical spectrum analyzer is the most widely used interrogation method for FBG based sensors. However, OSA and broadband source are bulky and expensive equipment and plenty of data need to be processed using this interrogation method to locate the Bragg wavelength peaks. Therefore, different interrogation method for FBG based sensors are proposed to improve interrogation efficiency.

One of the interrogation methods is based on Fabry-Perot (FP) tunable filter. A broadband light source and a FP filter are used in this measurement system. The reflected light from FBGs is filtered by the FP filter and then launch into photodetector. The center wavelength of the FP filter is chosen at the decline or rising edges of the reflected spectral curve. During measurement, the filter will transmit a variable power due to the reflected wavelength shift which can be expressed by convolution of spectral curves for FP filter and reflected spectral curves from FBG as equation: $F_{FP}(\lambda)*F_{FBG}(\lambda)$. Thus, Bragg wavelength shift can be told by measuring the power variation to the photodetector.

Another widely employed interrogation approach is using a tunable or swept-wavelength light source as the incident light and a photodetector to detect the reflected optical power from FBG. The input light usually has a narrow bandwidth or is single wavelength. When the input wavelength is swept to the center wavelength of FBG, the reflected power get to the maximum value. Thus, the center wavelength of reflected spectra can be detected by power measurement.

Besides, to obtain high speed and high resolution interrogation for multiple FBG sensor system, interrogation methods based on time stretch method have been proposed. A mode-locked fiber laser is used as a pulsed optical source, dispersion modules is used to map wavelength to time as a time-stretch scheme. Then the signal can be detected and processed by an oscilloscope. This method is accomplished by stretching the pulse in time to make the interrogation accuracy significantly increased.

CHAPTER 3

CONTACT FORCE SENSING FOR BIOMEDICAL CATHETERS

3.1 Introduction

Although contemporary cardiac electrophysiology (EP) procedures are routinely performed with minimal morbidity and mortality, perforation of either the vasculature or a cardiac chamber with catheters is an ever present danger. Catheters are usually put into human body far away from the targeted organ and have to travel through human organs and vessels, and perforations can happen during this process arisen from excessive force from a catheter, which could lead to devastating complications [27]. Furthermore, 3D electroanatomical mapping systems are also commonly used in cardiac EP procedures that an electroanatomical map is created by moving a catheter with bipolar electrodes throughout the chambers of the heart, collecting local electrograms (EGMs) at each point the bipole is in contact with the myocardium. These EGMs are then integrated together to create a 3D temporal-spatial representation of an arrhythmia. The accuracy of these maps is dependent upon the quality of the EGMS, which in turn is dependent upon the electrodes having adequate contact with the myocardium. Excessive contact with the myocardium, in contrast, could also cause perforation. Therefore, a catheter that is capable of measuring contact force during a procedure is essential to prevent unexpected damages to the organs [28]. Moreover, MRI guided technology in is also widely used EP catheter ablation which requires the sensing device immune to electro-magnetic interference, while most electronics based sensors do not fulfill this requirement [29].

Temperature insensitivity is another essential feature for accurate force measurements during procedures, like in an EP radio frequency ablation, where electrical energy is used to destroy tissues in the heart that are causing rhythm disturbances. This procedure causes an increase in temperature of the targeted area, disabling the function of any temperature sensitive FBG based force sensor. An ideal catheter based force sensor for real-time and temperature insensitive measured is highly desired in this situation.

Fiber optics based sensors have been intensively studied and widely used in various applications due to its unique advantages such as small size, electromagnetic interference immunity, and high sensitivity [1,10], which make it a perfect candidate for force sensing during EP procedures [30,31]. One example of fiber optics based force sensor is based on Fabry-Perot structure, in which the optical reflectance varies with optical cavity depth, while contact force or pressure determines the optical cavity depth [32,33]. Another method is based on light intensity modulation where light intensity is changed when the distance of a reflector is changed due to force applied at the catheter tip [34,35]. Unfortunately, the above approaches either require a special fabrication process to embed an elaborate cavity in the catheter tip or are sensitive to temperature change. Among different types of fiber optics based sensors, FBG is one of the most popular technology due to its high performance, simple structure, low-cost and maturity. While its applications on EP catheters have not been fully explored. One of the reason is FBGs are also excellent temperature sensors because the reflection wavelength shifts with any temperature change. Unfortunately, this imposes a significant limitation when using FBGs for force sensing because FBG force sensing relies on the measurement of wavelength shift to determine the amount of force applied onto the catheter and the corresponding organ, and both temperature and contact force create wavelength shift making them indistinguishable from one another [26]. Thus, a

temperature insensitive contact force sensor for EP catheters is highly desired to ensure reliability and high fidelity sensing in a medical procedure.

In this chapter, we develop FBG based contact force sensors for three types of most commonly used catheters: mono-directional steerable catheters, bi-directional steerable catheters, and non steerable catheters. Based on the different designs of the catheters, we demonstrated three different FBG based approaches for achieving contact force monitoring in all three types of catheters. Temperature sensitivity of the all the proposed sensors are also investigated.

3.2 Direct Power Measurement for Mono-directional Steerable Catheters

As such, the following work is drawn from our paper published on IEEE sensors journal (vol.16, pp. 4771-4775, June 2016) by Li Xu, Matthew I Miller, Jia Ge, Kent R Nilsson, Zion Tsz Ho Tse and Mable P. Fok entitled "Temperature-insensitive fiber-optic contact force sensor for steerable catheters".

Steerable catheters are commonly used in EP procedures to enable controlled-bending of the catheter, so that it can travel smoothly along human vessels and organs, which are twisty and supple [36]. Although Fiber optics FBG based force sensors are developed and different structures of FBG based catheter sensors are demonstrated [37-40], there is no research studying contact force measurement in steerable catheters where different curve diameters may occurs during an operation. Curve diameter is the furthest distance the catheter moves from its straight axis as it is deflected. Catheter steering has not been taken into account during force measurement; however, this capability is essential since catheters often need to be steered into various positions to fit human vessels and organs. Studying contact force measurement of a steerable catheter with various curve diameters is important because steering of catheter will create a change in the FBG reflection

spectrum which consequently affects the force measurement results. Thus understanding and utilizing the influence that curve diameter has on force sensing is essential for attaining accurate force measurements during a real medical procedure.

3.2.1 Experimental Setup and Principle

The first contact force sensor we present is a real-time temperature insensitive solution for contact force measurement in a steerable catheter. The measurement is achieved by measuring the total reflection power of the FBG sensor using an optical power meter. An FBG is fixed on the stretched side (outer arc) of a steerable catheter for contact force measurement and the catheter is then inserted into the catheter guide, just like during a medical procedure, as shown in Figure 3.1. The proposed FBG sensor does not require the use of an optical spectrum analyzer, instead, an optical power meter is used for measuring the total reflection power from the FBG. Since temperature variation will only shift the reflection spectrum but does not change the FBG reflection bandwidth, while contact force will change the refection bandwidth, the total reflection power is sensitive only to contact force but not the temperature variation. As a result, temperature insensitive contact force sensing is achieved by measuring the total reflection power from the FBG. Furthermore, the measurement of total reflection power does not require specific spectral information, which is a faster and simpler approach to acquire contact force information.

The proposed sensor is tested and calibrated under different amounts of curve diameter and temperature settings (12.7 ◦C to 65 ◦C), mimicking a real EP radiofrequency ablation scenario. Based on previous studies [41,42], the target contact force during ablation procedure is 20 g with a range of 10-30 g. Research has also shown that perforation could happen when the contact force

is as low as 77 g [43], while no perforation would occur when contact force is within the target range of 10 to 40 g.

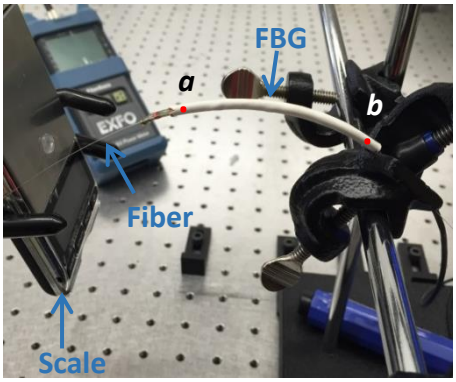

Figure 3.1. Experimental setup for contact force measurement with the FBG embedded steerable catheter sensor.

Figure 3.1 shows the FBG incorporated steerable catheter and the contact force measurement setup. In this approach, a non-magnetic 8 French EP catheter from St. Jude Medical Inc. is used, which is steerable to bend in a particular direction and is adjustable to have various curve diameters. The starting point of the deflectable section of the catheter is fixed on a holder to ensure the same onset location for bending to occur, mimicking the small entrance point of the catheter on a subject during an EP procedure. We set two points a and b at the beginning and end of the deflectable section of the catheter. The FBG is 14 mm long and is fixed in the middle of points *a* and *b* on the outer arc of the steerable catheter. A scale with 0.01 g resolution is used for measuring the applied contact force. A broadband light source is used as the light input to the FBG mounted on the steerable catheter, and an optical power meter (EXFO EPM-50) is used to measure the total reflected optical power from the sensor. The steering curve diameter is adjustable from 74.13 mm to 67.37 mm, as shown in Figure 3.2. Since the FBG is fixed on the outer arc of the catheter, it will have the same bending curvatures as the catheter during catheter bending.

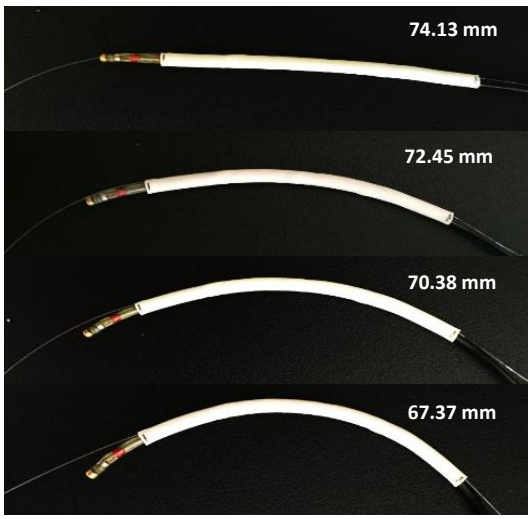

Figure 3.2. Different pre-bended curvatures of the steerable catheter.

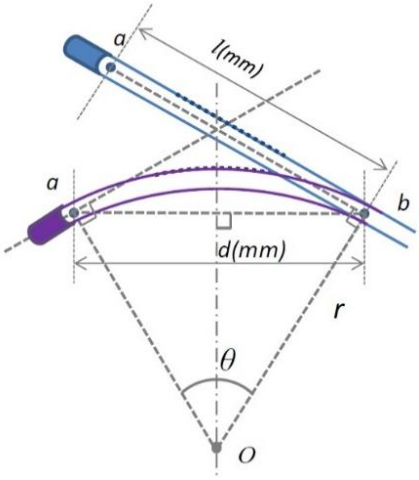

Figure 3.3. Schematic illustration of the steerable catheter without pre-bending (blue) and with pre-bending (purple). (b) Different pre-bended curvatures of the steerable catheter.

Figure 3.3 illustrates the steerable catheter without steering (blue) and after steering with a particular curve diameter (purple). We set two points, *a* and *b*, at the front part of the catheter where the bending occurs, while the FBG is located at the mid-point between *a* and *b*. We define the central angle between radiuses *aO* and *bO* as the bend curvature (θ) when contact force is

applied. The distance between *a* and *b* is the curve diameter (after steering is shown in purple), denoted as *d*, which can be measured easily and is directly related to the bend curvature θ and the fixed value of *l*, which is the distance between *a* and *b* without pre-bending (shown by the catheter in blue in Figure 3.3).

When force is applied onto the catheter tip, bending of FBG due to the elastic property of the catheter occurs, which leads to non-uniform stretching in each grating pitch of the FBG. The grating pitch governs the Bragg wavelength λ_B (reflection wavelength) of the FBG and is described by a well-known equation $\lambda_B = 2n_{eff} \cdot \Lambda$, where Λ is the grating pitch and n_{eff} is the effective index of the fiber core. Thus, stretching of the FBG results in an increase of pitch length that makes the Bragg wavelength shift to the longer wavelength direction. The interesting part here is that since the FBG is fixed on the outer arc of the steerable catheter, when the FBG is bent due to the force applied to the catheter tip, non-uniform stretching of grating pitches is resulted, which in turn results in chirping of the FBG and a broadening in reflection spectrum towards longer wavelength direction. The different extent of spectral broadening under different amount of contact force enable the use of total reflection power for measuring the actual force applied to the catheter. The use of spectral broadening for determining force applied to the catheter also provides the benefit of temperature insensitive operation. The temperature change would lead to a change in the effective refractive index (n_{eff}) of the FBG [1] as well as a uniform thermal expansion of the grating periods (Λ). Since both the change in n_{eff} and Λ are uniform, these two factors would only result in a wavelength shift of the reflected peak, while the bandwidth of the reflection spectrum and the total reflected power stay the same. Since our approach only measures the total reflection power of the FBG, temperature induced peak wavelength shifts will not affect the measurement because only the reflection wavelength is shifted, neither the spectral width nor the reflection power is

changed. As a result, the measurement is independent of the temperature and only contact force induced spectral broadening will change the total reflection power.

3.2.2 Results and Discussion

Figure 3.4(a) shows the reflection spectra of the embedded FBG under different amounts of force applied to the catheter tip with a preset steered curve diameter of 72.45 mm, and the corresponding 3-dB bandwidth change of the reflection spectra is shown in Figure 3.4(b). The steered curve diameter is adjustable through the catheter control knob and is measured by an absolute digimatic caliper. To observe the change in optical spectrum, an optical spectrum analyzer with a 0.8 pm resolution is used for detail characterization during the experiment, which is not necessary for sensing. As shown in Figure 3.4(a) and Figure 3.4(b), bandwidth of the FBG reflected spectrum is broadened as the applied force increases, and the overall reflection wavelength shifts towards the longer wavelength direction. When the applied force is increased from 0 g to 65.4 g, a total center wavelength shift of 3.0 nm is observed and the 3-dB bandwidth increases from 0.29 nm to 0.73 nm. Due to spectral broadening of the FBG reflection spectrum, the total reflection power is increased from -20.02 dBm to -18.21 dBm, as shown by the pink line with upward triangles in Figure 3.5. The optical power change resulted from force applied to the sensor is significant, making it possible to achieve direct power measurement using an optical power meter for contact force sensing.

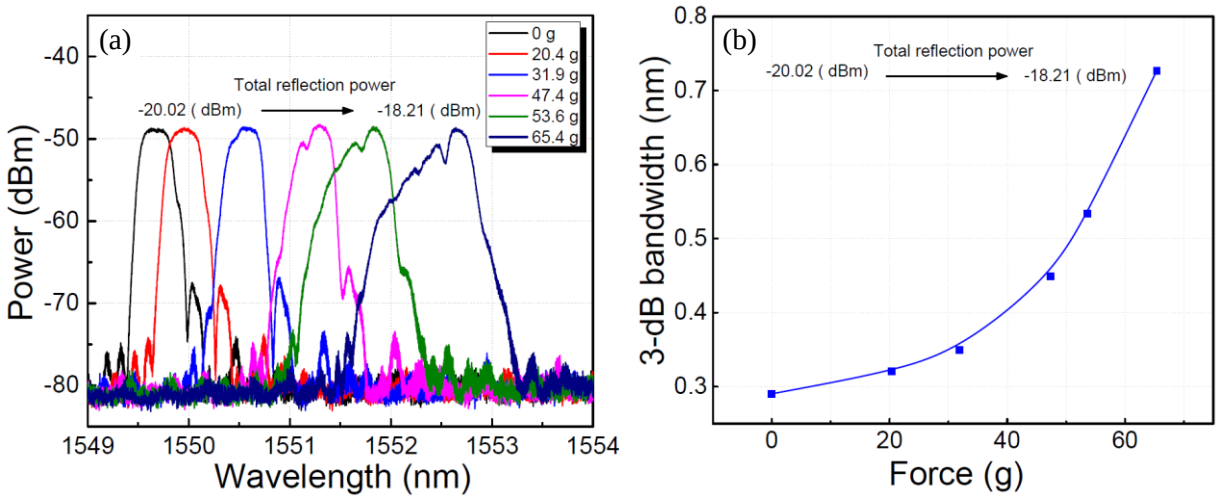

Figure 3.4. (a) Measured changes in spectral shape and spectral position of the FBG under different amount of applied forces with a pre-bended curvature of 72.45 mm. (b) Measured 3-dB bandwidths under different amount of applied forces.

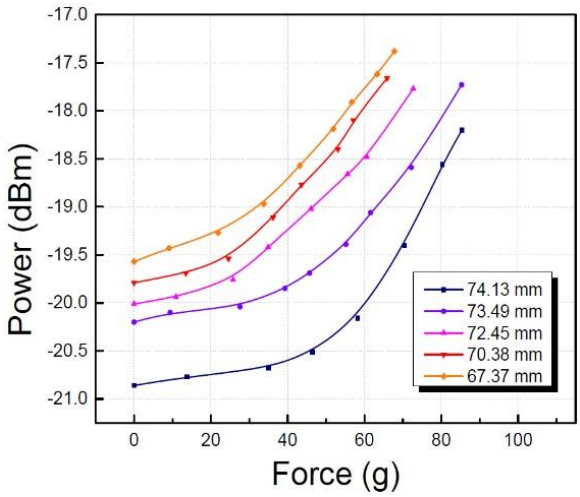

Figure 3.5. Measured total reflection powers of the catheter sensor under different amount of applied forces with various pre-bended curvatures of the steerable catheter.

Figure 3.5 shows the measured total reflection power of the FBG in response to different amounts of applied force at various initial steered curve diameters. Initial steered curve diameter

ranged from 74.13 mm to 67.37 mm is applied to the catheter before any contact force is applied, indicated by the first data point (at 0 g) in each curve. As displayed, the sensor has different initial reflection power for different initial steered curve diameters, varying from -20.86 dBm to -19.57 dBm. Therefore, calibration can be done based on Figure 3.5 when the catheter is steered at a particular curve diameter using the control knob, such that the actual contact force can be determined through optical power measurement. At each steered curve diameter, the total reflection power increases as the applied force increases with the same trend. The power change is significant enough to be measured by an optical power meter, such that no spectral information is needed. At a large steered curve diameter of 74.13 mm, the total power change is 2.66 dB when an 85.4 g force is applied to the steerable catheter tip. At a small steered curve diameter of 67.37 mm, the total power change is 2.19 dB when a 67.8 g force is applied.

When contact force is applied onto the catheter tip, bending of the catheter is observed depending on the initial steered curve diameter and the contact force applied to it. Catheter with smaller initial steered curve diameter experiences larger bending under the same amount of applied force. As shown in Figure 3.5, catheter with a large initial steered curve diameter (i.e. 67.37 mm) meets its bending limitation at about 65.0 g of applied force due to the over-bending of the catheter and the bending limitation of FBG. To prevent over-bending, the measured steered curve diameter is ranged from 74.13 mm to 67.37 mm and the applied contact force is ranged from 0 g to 65.0 g. Based on former studies, 65.0 g is enough for most EP procedures. When contact force is applied, the larger the bending, the larger the broadening in spectrum, and therefore a larger change in reflection power as well as a higher sensitivity are resulted, which explains the nonlinear power vs force relationship as shown in Figure 3.5. Furthermore, our approach has better absolute sensitivity than conventional wavelength measurement approaches. Taking an initial steered curve diameter

of 72.45 mm as an example, a sensitivity of 0.031 dB/g is observed for contact force of 72.7 g. Thus an absolute sensitivity of 0.032 g is resulted when an optical power meter with resolution of 0.001 dBm (OTM-300 series optical MultiMeter) is used, which is improved compare with the conventional techniques. It is worth noticing that once the contact force is removed, both the steered curve diameter and initial total reflection power are restored to their initial values. Furthermore, the contact force measurement is highly repeatable that shows the reliability of the proposed FBG force sensor incorporated steerable catheter.

To investigate the temperature dependency of the proposed FBG incorporated steerable catheter, the catheter is immersed in a water bath with various temperature. Figure 3.6 shows the measured total reflection power of the FBG sensor at different testing temperatures. Temperatures ranging from 12.7 ◦C to 65.0 ◦C were tested which covers the whole potential temperature range that EP procedures may reach. As shown, the total change of reflection power is smaller than 0.2 dB, which proves the temperature insensitive capability of the proposed sensor measurement scheme. The 0.2 dB of variation could be resulted from thermal expansion of the catheter guiding tube and the accuracy of the optical power meter. This temperature insensitivity can be further explained by the optical spectral profiles of the FBG sensor. Since temperature change will result in a shift in FBG reflection wavelength, the FBG reflection spectra shown in the inset of Figure 3.6 are normalized in wavelength with actual measured power, for comparing the FBG reflection profiles at various temperatures. When temperature is changed from 12.7 ◦C to 65.0 ◦C, no change in reflection bandwidth or spectral profile is observed, indicating that the corresponding total reflection powers are the same. The good temperature insensitivity of the proposed catheter sensor provides accurate and reliable contact force measurement during EP procedures.

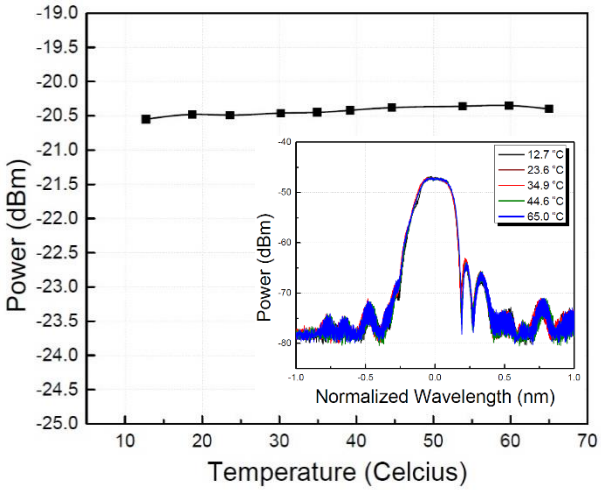

Figure 3.6. Measured total reflection powers of the catheter sensor with respect to different temperatures. Inset: Corresponding reflection spectra of the FBG at different temperatures.

3.2.3 Summary

A steerable catheter with an incorporated FBG sensor for contact force measurement is studied experimentally under various steered curve diameters and contact forces. The applied contact force value is obtained through direct measurement of the total reflection power from the FBG using an optical power meter, such that real-time contact force monitoring is achieved without the need for analyzing the spectral information of the FBG. Since the temperature change induced wavelength shift in reflection spectrum will not affect the reflection power of the FBG, the proposed scheme is insensitive to temperature influence. The relationship between the total reflection power, steered curve diameter, applied contact force, and temperature change are studied. The results show that reflection power change due to contact force applied has the same trend when different initial steered curve diameters are set through the catheter control knob. As a result, the actual force applied to the catheter during a procedure can be determined easily through calibration using the control knob information. This design provides a practical and compact

solution for real-time contact force measurement during EP procedures, which is suitable for various biomedical applications.

3.3 FBG-Pair Scheme for Bi-directional Steerable Catheters

As such, the following work is drawn from our paper published on IEEE sensors journal (vol. 17, pp. 5118-5122, Aug. 2017) by Li Xu, Leah A Feuerman, Jia Ge, Kent R Nilsson, Zion Tsz Ho Tse and Mable P. Fok entitled "Temperature-Insensitive Contact Force Sensing in Bi-Directional Catheter Using Fiber Bragg Grating Pair".

Another type of steerable catheter is bi-directional catheters, that the catheter can be controlled to bend into two opposite directions. A bi-directional catheter is deflectable, which enables the operator to move it in two opposing directions. This type of catheters are commonly used in electrophysiology mapping and ablation procedures. In this section, we design and demonstrate a temperature and deflection angle insensitive sensor for the contact force measurement in bi-directional catheters. A FBG pair consists of two FBGs with the same center wavelength (i.e., overlapped spectrum). The pair can be used as a sensor by fixing the two FBGs on opposite deflection arcs of the bi-directional catheter. When contact force is applied to the catheter tip, spectral bifurcation is observed in the reflection spectrum of the FBG pair, resulting in two reflection peaks in the spectrum. The spectral separation between the two reflection peaks increases linearly as the contact force increase. Although catheter deflection will also cause spectral bifurcation, the change in spectral separation between the two peaks is independent of the deflection angle (i.e., curve diameter). Furthermore, unlike the conventional approach where the absolute wavelength shift is used to quantify the applied contact force, our approach measures the change in spectral bifurcation in response to the application of contact force, which is a temperature

insensitive solution. The proposed sensor incorporated with a bi-directional catheter is tested with different amounts of contact force, from 0 to 60 g at various deflection angles and directions, which cover the target contact force range that could be used in surgery. Contact forces larger than our measurement range, 0-60 g, can be considered as having risk of perforation. The independence to deflection angle for the two bending directions and temperature insensitivity properties represent a reliable contact force sensing approach for EP procedures.

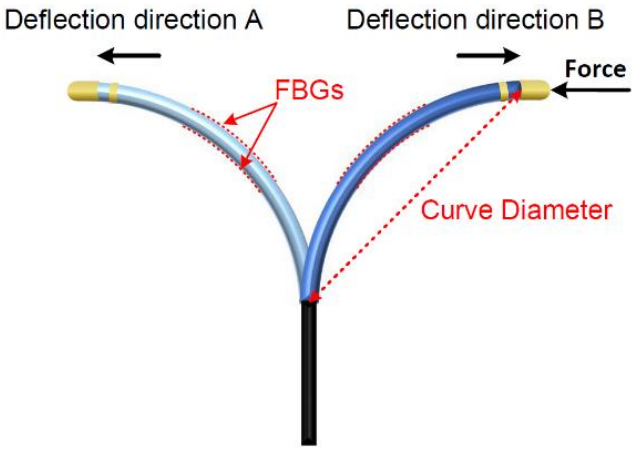

Figure 3.7. Illustration of the FBG-pair embedded bi-directional catheter.

3.3.1 Experimental Setup and Principle

Figure 3.7 illustrates the FBG pair embedded bi-directional catheter with the red dashed lines indicating the position of the FBG pair. A 1304-7-25-M-BD therapy bi-directional ablation catheter from St. Jude Medical Inc. was used, which is deflectable in two opposite directions (A and B in Figure 3.7) with various curve diameters. Curve diameter is the furthest distance the catheter moves from its straight axis as it is being deflected. Two FBGs with the same center wavelength (1550 nm) were embedded on the opposite sides of the bi-directional bend region. Contact cement super glass glue was used to fix the FBGs for demonstration, which is sticky and flexible enough to allow the FBGs to bend with the catheter while still securely attaching to the

catheter during deflection. The catheter is deflectable in two opposite directions through the integrated control handle. When contact force is applied onto the catheter tip, the catheter is bent slightly due to its flexibility, resulting in a decrease in curve diameter. Therefore, the FBG embedded on the inner arc is compressed while the one on the outer arc is stretched due to the elastic property of the catheter. The stretching/compressing of the FBGs lead to a change in grating pitches, which in turn results in a change in the FBG Bragg wavelength λ_B. This phenomenon is described by equation $\lambda_B = 2n_{eff} \cdot \Lambda$, where Λ is the grating pitch and n_{eff} is the effective index of the fiber core. Therefore, Bragg wavelength of the inner arc FBG (compressed) is decreased while that of the outer arc FBG (stretched) is increased, resulting in spectral bifurcation as shown by the red curve in Figure 3.8. Two distinct peaks were observed in the spectrum, and the separation between the two peaks was used to characterize the amount of contact force applied to the catheter. An increase in contact force decreased the curve diameter of the catheter, thus, increasing the amount of compression and stretching at the FBG pair which in turn increased the separation between the spectral peaks. If an FBG is embedded on the side direction of the catheter insdead of along the steered bending direction, due to the pure bending model, the FBG is not being stretched or compressed. Thus, the Bragg wavelength can not be changed by the bending of catheter.

Figure 3.8 shows an example of the FBG-pair optical spectrum before contact force was applied (black) and after contact force was applied (red). This example corresponds to a contact force of 21.6 g and a 1.05 nm difference between the peaks. Based on the same principle, when the catheter is deflected to either direction through the control of the deflection handle, spectral bifurcation is also observed. When contact force is applied after the catheter is deflected, a further increase in spectral peak separation is resulted. Therefore, the effect of the contact force can be

determined by measuring the change in spectral peak separation when contact force is applied, which is independent of the amount of deflection.

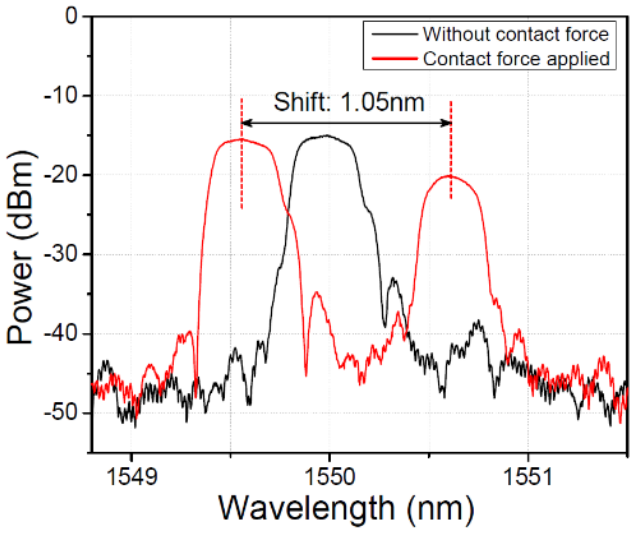

Figure 3.8. Measured wavelength shift before (black) and after (red) contact force applied.

To calibrate the relationship between contact force and change in FBG peak separation, a digital scale with 0.01 g resolution and 300 g capacity was used for measuring the contact force. A broadband light source from 1290 nm to 1660 nm (S5FC1005S Superluminescent Diode (SLD) Source from Thorlabs Inc.) was used as the input light to the FBG pair. An optical spectrum analyzer (APEX AP2040A) with 0.8 pm resolution was used to capture the reflected light from the FBGs through a circulator for spectral measurement and wavelength shift measurement.

It is worth noting that any temperature change will affect the reflective index n_{eff} of the FBG, which in turn causes a shift in FBG reflection wavelength according to the equation $\lambda_B=2n_{eff}\cdot\Lambda$. Our proposed scheme is designed to use the change in peak separation instead of an absolute wavelength shift to characterize the amount of contact force. Therefore, any temperature change will have the same effect on both the FBGs in n_{eff} as well as same magnitude and direction in wavelength shift in the FBG pair. As a result, temperature will not affect the resultant peak

separation. Thus, the proposed FBG pair approach is temperature insensitive, which is a highly desired property in contact force measurement during EP procedures. Temperature dependence of the proposed contact force sensor is studied by setting a water bath at various temperatures during force measurement. The FBG-pair embedded catheter is immersed into the water bath while the temperature is monitored by a thermometer (HI98509 - Checktemp®1C). Hot water is added into the container to increase the temperature of water bath.

3.3.2 Results and Discussion

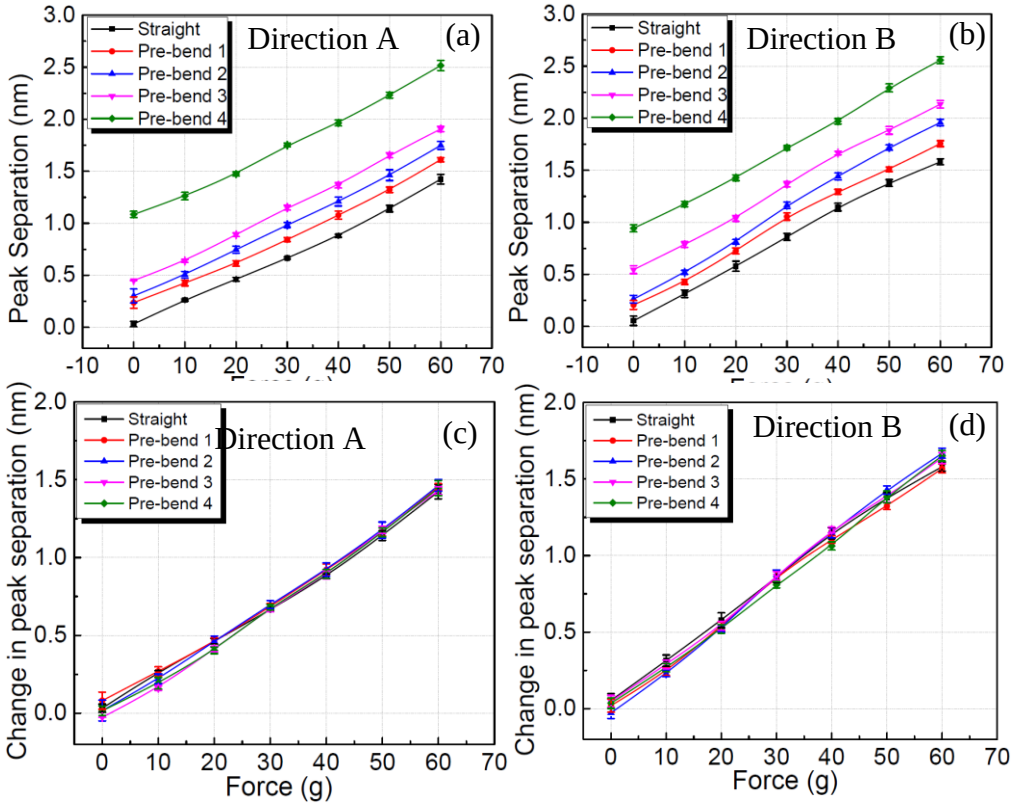

Figure 3.9. (a)-(b) Measured Bragg wavelength differences between the two FBGs with various applied contact forces for deflection direction A and deflection direction B. (c)-(d) Change in peak separation with error bars for bending direction A and bending direction B.

The spectral peak separation (i.e. Bragg wavelength differences) of the FBG pair under different amounts of contact force is measured with no deflection in the catheter (refer as straight) and with deflection at both A and B directions. Figure 3.9(a) and 3.9(b) show the measurement results for deflection direction A and deflection direction B, respectively. A linear relationship between the spectral peak separation and the contact force is observed when the applied force is increased from 0 g to about 60 g. Since the amount of preset catheter deflection also contributes to spectral bifurcation, an increase in initial spectral peak separation is observed at 0 g force as deflection increases. Increase in deflection means a decrease in curve diameter; therefore, the corresponding spectral peak separation is increased. Curve diameters of 64.95 mm (pre-bend 1), 61.33 mm, 58.03 mm, and 55.31 mm (pre-bend 4) are used for the investigation. Although deflection at the catheter causes a change in initial spectral peak separation, the general linear trend between the spectral peak separation and the contact force can still be observed. Therefore, by plotting the relationship between the change in spectral peak separation and the contact force, a consistent linear relationship is observed that is independent to the amount of deflection, as shown in Figure 3.9(c) and 3.9(d). The slopes of all the curves with different amounts of deflection are similar with small errors of 0.01 - 0.02 nm, which is contributed from the error during spectral peak search. Our FBG pair has a spectrum with a relatively flat top, thus, we expect that the measurement error can be improved with the use of FBG pair with sharper peaks. This deflection independent capability of our approach is a significant improvement over former research [6] introduced in the previous section, and will greatly simplify the measurement process in real applications. The FBG pair has a minimum measurable curve diameter of 47.9 mm, and the largest contact force we can measure is about 60 g, which exceeds what is needed in EP procedures. A smaller curve diameter or larger contact force than the limit may cause over stretching of the FBG

and affect the accuracy of the measurement. The measurement sensitivity of deflection direction A is about 0.025 nm/g and that of deflection direction B is about 0.032 nm/g. The error in force measurement can be calculated from the sensitivity, wavelength error of 0.01 - 0.02 nm which corresponds to a force error of 0.4 g - 0.8 g for direction A and 0.3125 g - 0.625 g for direction B. Since the FBGs used in this experiment have the same center wavelength but are not spectrally identical, the corresponding sensitivities for each deflection direction is slightly different.

Temperature insensitive capability is extremely important for reliable contact force sensing at the catheter because heat is generated at the tissue during radio frequency ablation in EP procedure. Temperature change will cause the Bragg wavelength of the FBG pair to shift in the same direction by the same amount. Therefore, a change in temperature will only shift the whole bifurcated spectrum to one direction while maintaining its spectral peak separation as if there is no temperature change. Figure 3.10(a) shows the measured optical spectra of the FBG pair with a 56.82 mm preset curve diameter. The black curve represents force sensing at 33.9 ◦C while the red curve represents force sensing at 36.6 ◦C. As shown, both the Bragg wavelength peaks shift to the longer wavelength direction by 0.12 nm while the spectral peak separation is maintained at 0.68 nm despite the temperature change. The spectral peak separations under different temperature conditions between 18.7 ◦C to 61.5 ◦C is shown in Figure 3.10(b), the range is selected to cover all possible temperature conditions that occur in EP procedures. The spectral peak separation is kept constant with a fluctuation of less than 0.05 nm for a temperature range between 18.7 ◦C to 61.5 ◦C. The obtained consistent spectral peak separation proves the temperature insensitivity property of the proposed approach, which provides accurate and reliable contact force measurement.

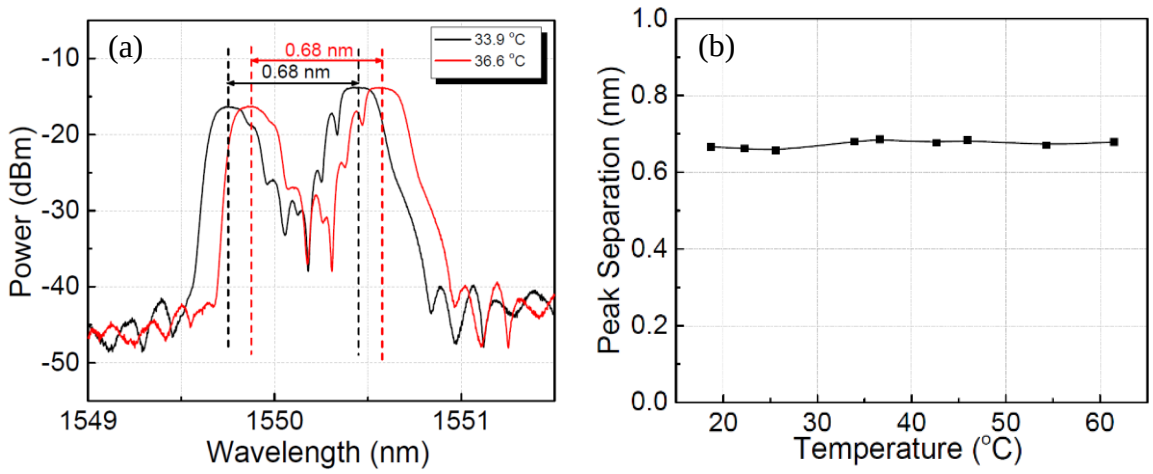

Figure 3.10. (a) Wavelength shift for the two FBGs at different temperatures. (b) Measured Bragg wavelength difference at various temperatures.

3.3.3 Summary

An FBG pair with the same Bragg wavelength is embedded on two opposite deflectable sides of a bi-directional catheter at the deflection area. Spectral bifurcation is observed when contact force is applied to the catheter tip, and the spectral peak separation in the FBG pair increases as the contact force increases. The experimental results show a linear relationship between the amount of contact force applied and the resultant spectral peak separation of the FBG pair. The effect of catheter deflection on the contact force measurement is decorrelated by using the change in spectral peak separation as an indicator for the amount of contact force applied. Therefore, no further calibration is needed for different deflection angles and directions. The demonstrated scheme is also temperature insensitive since temperature will only shift the FBG-pair Bragg wavelength to the same direction but have no effect on the spectral peak separation. The largest contact force measured in the experiment is about 60 g, which covers the amount needed during EP procedures. The presented approach is a reliable solution for practical contact

force measurement in bi-directional catheters, which can be used in catheters for EP mapping, ablation procedures, and implant delivery.

3.4 Spirally fixed FBG Scheme for Non-steerable Catheters

As such, the following work is drawn from our paper published on Optics express (vol. 22, pp. 10439-10445, May 2014) by Jia Ge, Hanlin Feng, Yue Chen, Zion Tse Ho Tse and Mable P. Fok entitled “Spiral-structured fiber Bragg grating for contact force sensing through direct power measurement”.

The third type of EP catheters is non-steerable, that the bending of the catheter can not be intentionally controlled. For this type of catheters, since the bending direction is not known, contact force sensors on the catheter must be able to response to any bending directions. In this section, we demonstrate a compact force sensing system through direct optical power measurement. The proposed sensor is insensitive to the bending directions of the catheter, making it suitable for non-steerable catheters. Our approach uses a standard FBG that is spirally fixed onto a catheter, such that the sensor can response to any bending directions of the catheter. When force is applied to the FBG sensor, the unique spiral structure leads to FBG chirping and reflection spectrum broadening. Only a laser source and a power meter are used to interrogate the applied force, which significantly reduces system complexity and cost.

3.4.1 Experimental Setup and Principle

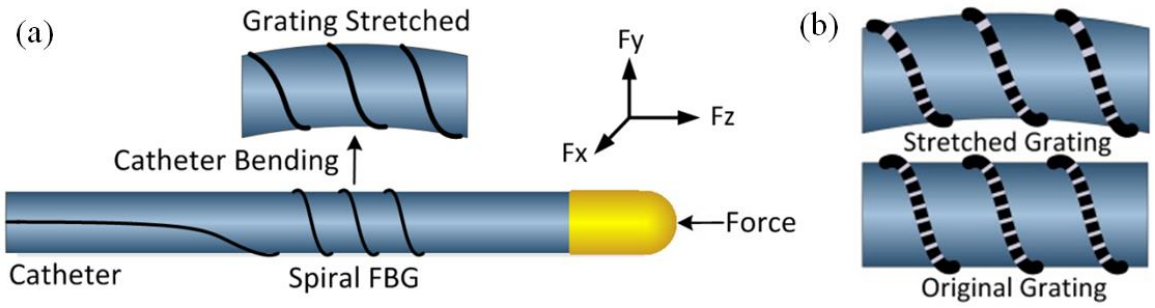

Figure 3.11. (a) Illustration of the spiral-structured FBG force sensor mounted on a catheter. (b) Corresponding change in grating pitches under the influence of applied force.

In the conventional force sensor where the FBG is placed in parallel with the target object, only the peak reflection wavelength λ_B is shifted significantly under different applied force, while the reflection bandwidth is remained unchanged. To determine the strength of force applied to the FBG, the amount of λ_B shift has to be measured, which typically involve the use of OSA and BBS. In our approach, a standard FBG is used for force measurement, which is spirally fixed onto a thin tube (e.g. a catheter) as illustrated in Figure 3.11(a). With the spiral structure, chirp effect is introduced to the FBG when force is applied, resulting in a broadening in spectral shape and reflection bandwidth. Compare with a parallel structure, the spiral structure enhances the bending of FBG and resulting in a more significant chirping effect. It has been shown that the chirping can be induced to a standard FBG and the reflection spectrum bandwidth can be adjusted by displacing one end of FBG in axial direction with the other end fixed [44] or by fixing the FBG onto a support beam with slanted direction and changing the beam curvature [45]. When force is applied onto the catheter tip, it is effectively transferred to the bending of the FBG sensor area due to the elastic property of the catheter. Since the FBG is mounted spirally onto the catheter, bending of the

catheter results in uneven changes in each of the grating pitch length Λ at different positions, most are stretched in different extends and some are kept unchanged, as illustrated in Figure 3.11(b). Stretched gratings with longer pitch length Λ lead the λ_B shift to longer wavelength direction, as a result, the non-uniform stretching of grating pitches lead to FBG chirping, providing a broadened reflection spectrum towards longer wavelength direction and slower ramp edge at shorter wavelength side, as illustrated in Figure 3.12(a). Due to the spiral structure, the stretching of FBG is non-uniform, most of the gratings are stretched in different extends and contributes to the broaden reflection spectrum at the longer wavelength as well as a stronger reflection. Only a small portion of gratings keep unchanged, resulting in the slow ramp profile at shorter wavelengths and a weaker reflection, similar results can be found in previous research [45].

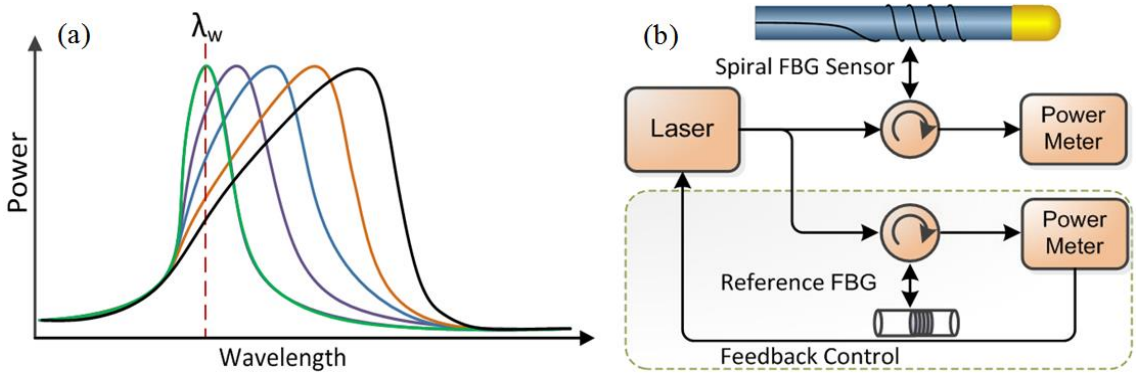

Figure 3.12. (a) Illustration of the change in spectral shape under different amount of applied force. (b) Measurement system for the spiral-structured FBG force sensor.

Instead of measuring the reflection wavelength shift, our approach makes use of the change in spectral shape of the FBG and performs direct power measurement. As indicate in Figure 3.12(a), the slope of the slow ramp edge at shorter wavelength changes as the applied force increases. Thus, the amount of applied force can be determined by measuring the reflection power at a particular wavelength at the slow ramp edge. This is achieved by launching a single

wavelength laser light (at λ_w) into the FBG through a circulator and measure the reflection power using an optical power meter, as shown in Figure 3.12(b). The basic system consists of a laser source, an optical circulator, and an optical power meter, while the part inside the dotted box is for temperature effect mitigation. To result in high sensitivity, λ_w is picked such that the difference in reflection power is the largest under different amount of applied force, as illustrated by the red dotted line in Figure 3.12(a).

In the experiment a non-magnetic EP catheter with a radius of 4 mm is used as the fixture, which is fabricated in a way that it is slightly bent in one particular direction. Thus, when force is applied to the sensor in F_z direction, the catheter always bends to the same particular direction. Moreover, one end of the catheter is fixed so that the bending position is also the same when force is applied. A 35 mm long FBG is fixed in the middle of the catheter (the bending position), with 12 mm spiral pitch gap. In order to prevent breakage and to reduce bending loss of the FBG, the grating area is wrapped around the tube at an angle of about 40˚ with respect to the catheter. A DFB laser (ILX Lightwave 79800) at 1549.9 nm with +5 dBm power is used as the laser beam for launching into the spiral FBG sensor, and an optical power meter (EXFO EPM-50) is used to measure the reflected optical power. Compare with conventional sensing systems based on OSA and BBS, our approach does not require capturing the entire spectrum for determining the wavelength shift. Thus, our approach is simple, compact, consumes less computation power, and has low latency.

3.4.2 Results and Discussion

Figure 3.13(a) is the measured reflection spectra of our proposed spiral-structure FBG sensor. The spectra are measured under different contact forces ranging from 0 to 1.55 N, with

0.15 N force differences for each curve. An amplified spontaneous emission BBS is used as the input light and an OSA with a resolution of 0.8 pm (APEX AP2040A) is used for capturing the spectra. This setup is for comparing the change in spectrum and is not necessary for force measurement in the spiral-structure FBG sensor.

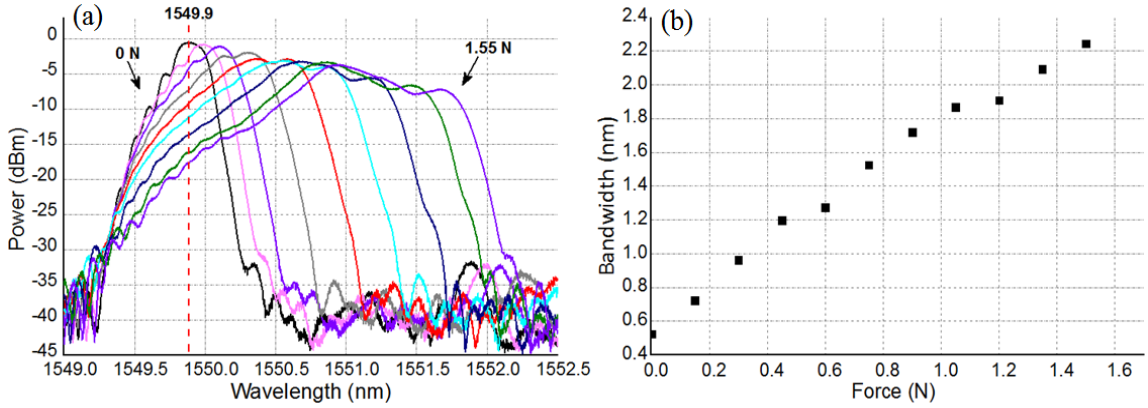

Figure 3.13. (a) Measured FBG reflection spectra under different amount of applied force. (b) Reflection bandwidth of the FBG under different amount of applied force.

As shown in Figure 3.13(a), peak reflection wavelength of the spiral structure FBG is shifted by ~1.5 nm and significant broadening in reflection bandwidth is observed when force is applied to the catheter. There is a slight decrease in the maximum power at the spectrum peak, but the total reflection power is increased due to the broadened spectrum. The entire reflection spectrum moves toward the longer wavelength direction, at the same time, the ramp profile at the shorter wavelength gradually gets broader as the strength of applied force increases, while the longer wavelength side stays steep. The slow ramp profile is caused by the non-uniform stretching of most grating pitches in different extends and only a small portion of gratings keep unchanged, thus, the change of reflection power at different wavelength is uneven. Figure 3.13(b) shows the measured reflection bandwidth under different amount of applied force, which is determined from

the original spectra in Figure 3.13(a). With an increasing applied force, the reflection bandwidth gradually increases by ~1.7 nm, i.e. from 0.5 to 2.2 nm.

The significant change in the slow ramp profile shown in Figure 3.13(a) becomes the ideal region for discriminating changes in the FBG spectrum under different amounts of applied force, because the optical power reflected at a particular wavelength is different under different amounts of applied force. In general, the peak reflection wavelength λ_B of the original reflection spectrum (at 0 N, indicated by the red dashed line in Figure 3.13(a)) is the optimal working wavelength λ_w. At this wavelength, the measured power is at maximum value when no force is applied and a monotonically decreasing curve can be obtained under increasing applied force. It also has the largest power change for discriminating the amount of applied force and resulting in highest sensitivity.

Figure 3.14 is the measured power response against different amounts of applied contact force, ranging from 0 to 1.55 N. The DFB laser has very good stability in terms of power and wavelength, corresponding fluctuations are less than 0.01 dB and 0.001nm, respectively. The reflected insertion loss of the whole system (most from the spiral FBG) is 4.7 dB, remains unchanged during measurement. Under an applied force from 0 to 1.55 N, the reflection power is decreased from 0.3 to -17 dBm, resulting in an average sensitivity of 11.16 dB/N. The sensitivity is significantly better than previous power measurement approaches. A good discrimination of applied force with a step interval of 0.025 N is experimentally achieved among the whole test range, resulting in a measurement resolution of 0.025 N. As shown in Figure 3.14, a proportional relationship is found between the applied force and reflection power, with a linear fit R2 of 0.98216 in dBm unit. The proportional relationship and linear fit allow simple conversion from reflected optical power to the amount of applied force, enabling fast signal processing speed and real-time

measurement. The sensor meets it's limitation at 1.55 N due to the over-bending of catheter under a strong contact force, with a maximum bending radius of ~5 cm. The reflection power is back to 0 dBm when the applied force is removed and the measurement system has a good repeatability.

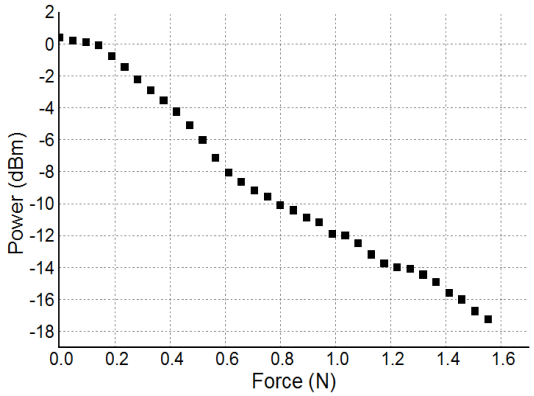

Figure 3.14. Measured reflection optical power of the spirally structured FBG at different amounts of applied force.

Temperature induced spectral shift is an undesired behavior and has general influence to all FBG sensors, which would significantly affect sensing accuracy. Figure 3.15(a) and 3.15(b) show the reflection spectra of the spiral FBG at different temperature (from 20 to 60 ˚C with an interval of 10 ˚C) under a fixed force of 0 and 1.0 N, respectively. An increase in temperature results in spectral shift to the longer wavelength direction, while the spectral shape and reflection power is kept unchanged. Compare with Figure 3.15(a) and 3.15(b), the amount of temperature induced wavelength shift is almost the same (~0.4 nm) when different amount of force is applied to the spiral-structured FBG. In our approach, temperature influence can be compensated using a similar FBG as a reference grating, which has the same original Bragg wavelength as the spiral FBG. The temperature compensation scheme is illustrated in the dotted box in Figure 3.12(b). The reference grating is fixed near the catheter but no force is applied onto it. This reference grating shares the same laser source by splitting the laser output with an optical coupler. Temperature

change shifts the reflection wavelength of both the spiral FBG and the reference FBG by the same amount. Thus, the wavelength shift resulted from temperature fluctuation can be reflected by power measurement at the reference grating. The power information of the reference grating can be used to tune the laser wavelength to be aligned to the reflection peak of the reference grating as well as the spiral FBG, which is the new optimized working wavelength resulted from temperature change. Figure 3.15(c) is results of the spiral structure FBG sensing system measured at different temperature ranging from 20 ˚C to 60 ˚C with temperature compensation. The power vs. force curves at different temperature settings are almost the same, proofing that the temperature effect is successfully compensated.

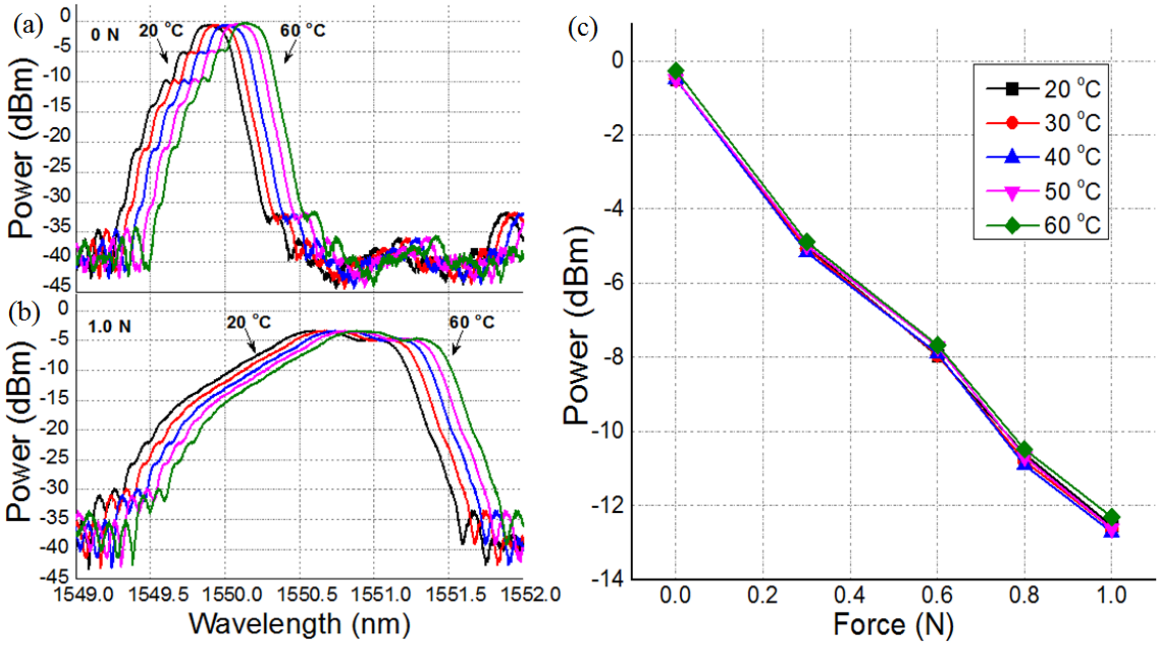

Figure 3.15. (a)(b) Spiral FBG reflection spectra measured at different temperatures under fixed force of 0 and 1.0 N. (c) Power measurement test at different temperatures with temperature compensation.

3.4.3 Summary

In summary, a high-sensitivity FBG contact force sensor is proposed and experimentally demonstrated. The measurement system requires only a laser source and an optical power meter. With a novel spiral FBG structure, we achieve a simple, compact, and high-sensitivity force measurement design through direct optical power measurement. A proportional relationship and linear fit are found between optical power and applied force up to 1.55 N, and an average sensitivity of 11.16 dB/N is experimentally achieved. Temperature influence has been studied and a reference grating is proposed for temperature effect mitigation. This design significantly reduces the system complexity and latency, as well as improves data processing speed, which has a great practical value in real-time FBG sensing applications.

3.5 Summary

In this chapter, we developed three FBG based contact force sensing schemes for different types of biomedical catheters. Direct power measurement of the total reflection power of an FBG contact force sensor is achieved for the mono-directional steerable catheters, an FBG-pair scheme is used to monitor the applied contact force for the bi-directional steerable catheters, and a spirally fixed FBG with chirped reflection spectrum is designed for the non-steerable catheters. Accurate contact force measurements are experimental demonstrated and calibrated for all three types of catheters. Furthermore, the temperature sensitivity of the all the proposed sensors are also studied. Temperature insensitive designs or temperature compensating schemes in normal operating conditions are incorporated to the proposed sensing schemes, making them capable of working under different temperature conditions. The proposed designs are tested on different EP catheters,

in principle, these schemes can also be applied to any cylindrical tube-like fixture for contact force measurement, which is highly desired in many minimally applications.

CHAPTER 4

FBG BASED SENSOR FOR SOFT ROBOTICS APPLICATIONS

4.1 Introduction

Curvature sensing, Three-Dimensional (3D) shape sensing and stretchable sensor are essential in a wide range of applications including structural health monitoring in civil engineering, motion detection of wearable devices, minimally invasive surgery and human body monitoring for biomedical purposes [46], as well as real-time sensing of soft robotic configuration [47]. In soft robotics, curvature, stretchable and 3D shape sensors are widely used for the real-time position and shape information estimation [48], while in minimally invasive surgery shape sensing focuses on orientation measurement along a 3D curve [49]. Human body monitoring requires a shape sensor to measure the shape and volumetric changes of the human body days or nights [50]. Conventional curvature and 3D shaper sensors are usually achieved through pressure measurement and space change measurement through electronic sensors. In recent years, several electronics based 3D shape sensors have been proposed to accomplish 3D geometry reconstruction [48,51], body shape change measurement [50], and surface shape measurement [49, 52]. However, electronics based approaches are usually interfered by electromagnetic signals, limiting their functionality and performance in extreme environment.

Fiber optic sensor research has been booming over the last decade [1-5 ,53] due to its unique advantages over conventional electronic sensors, including its light weight and tiny size, low transmission loss for long distance measurement, instant response, immune to electromagnetic

interference, chemically inert, and nontoxic, i.e. not harmful to human body as a in vivo sensor. The unique properties of fiber optic sensor make it a good candidate for soft robotics and biomedical application. Due to these unique features of fiber optics, fiber optics technique is considered as a promising candidate for curvature and shape sensing, and various approaches have been proposed in recent years. For curvature measurement, demonstrated methods include including the use of interferometric structure for phase modulation [54], specialty fibers with unique structures [55], and various types of fiber gratings [56-58]. For 3D shape measurement, most existing fiber optics approaches are limited to 3D curve sensing along a fiber or a line instead of surface shape sensing. One example is based on multi-core fiber [60] for demonstrating an orientation sensitive curve sensor. Another example is the tiled fiber Bragg gratings (TFBG) [61], where two planes of tiled FBGs with an orthogonal structure is used to accomplish a 3D curve sensing along the fiber. Although the interferometric structure and specialty fiber schemes are usually having a higher sensitivity than most other alternatives, they are not favorable for practical implementation due to the structure complexity and high fabrication cost.

On the other hand, the fabrication process of fiber grating is simple and mature, which has been well developed and widely used. Curvature sensors and shape sensors based on various FBG structures also show promising sensing capability. Examples include using a tilted FBG [61], splicing a standard FBG with a multimode fiber [57], using multi-FBG structure for respiration movement monitoring [58], and a static bending sensor based on FBG embedded shape memory polymers [59]. However, The above approaches either have a limited measurement range due to the requirement of strong glues for fixing the FBG, or incapable of distinguishing bending directions of a curvature. Thus, most of the FBG based approaches can only accomplish curvature and shape sensing along the fiber, instead of measuring a 3D object or surface. Although fiber

optics brings unique features to the sensor designs, these limitations greatly hinder their application, a 3D shape sensor for multi-point surface measurement is still highly desired.

In this chapter, we first developed an FBG based curvature sensor which is capable of measuring both the bending curvatures and bending directions of a curvature. The sensor is off-centered embedded in a silicone sheet, which is very soft and removes the need of any adhesives. The developed bi-directional curvature sensor is then used as the basic sensing element, and is put into a dual-layer orthogonal FBG mesh structure for achieving multi-point shape sensing. A soft 3D shape sensor is then developed with the capability of measuring the profile of both concave and convex surfaces. Furthermore, we also developed a stretchable sensor by embedding a sinusoidal-structured fiber Bragg grating in a silicone sheet at an off-center position, which uniquely enables 130% of stretching and facilitates strain, torsion direction, and curvature measurement.

4.2 Bi-directional Curvature Sensor

As such, the following work is drawn from our paper published on IEEE Photonics Technology Letters (vol. 28, pp. 2237-2240, Oct. 2016) by Jia Ge, Aneek Enrique James, Li Xu, Yue Chen, Ka-Wai Kwok and Mable P. Fok entitled “Bidirectional Soft Silicone Curvature Sensor Based on Off-Centered Embedded Fiber Bragg Grating”.

In this section, a compact bi-directional soft curvature sensor is achieved by embedding a FBG off-centered in a silicone sheet. The proposed approach is capable to distinguish both the bending curvatures and bending directions through wavelength shift measurement of the FBG. Based on the pure bending model, the relationship between the FBG embedded position and the sensor sensitivity is studied and verified experimentally. Real-time curvature measurement of both

positive and negative bending directions is experimentally achieved. The curvature sensor has a consistent performance and the results are highly repeatable with small variances. A linear relationship between applied curvature and FBG wavelength shift is obtained, with a large measurement range of up to ±80 m^{-1} curvature.

4.2.1 Design and Fabrication

To achieve real-time sensing with a large measurement range, the adopted sensor material must be soft enough to be bend freely with the testing objects, while the FBG must be fixed to the sensor material. The use of strong glues for fixing the FBG is not desired since the physical property of both the sensor material and the FBG will be affected. Here, we propose the use of silicone as the sensor material as well as the material to fix the FBG in position. Figure 4.1(a) shows the proposed soft silicone curvature sensor as well as the measuring setup, where FBG is embedded inside a flat silicone sheet and is fixed very well without using any adhesive. The FBG is centered along the *y*-direction in the silicone sheet coordinate but offset from the center in the *z*-direction. The cross-section view of the sensor, shown in Figure 4.2, indicates the silicone sheet acts as a solid media tightly interacting with the FBG under constant curvature deformation. Due to the soft property of the silicone sheet, it can be placed onto and complied with the tested objects along the exact same curvature profiles.

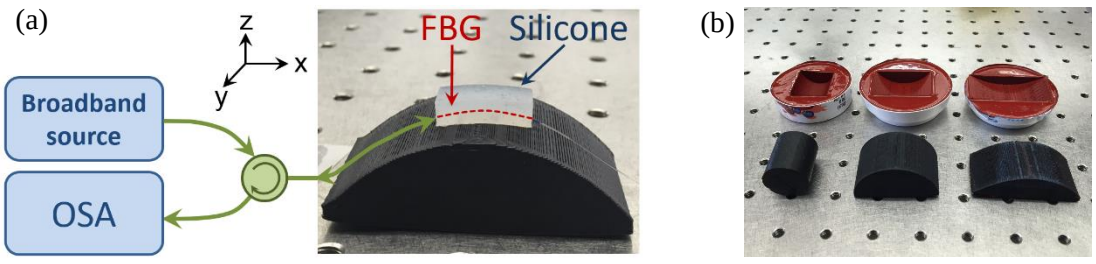

Figure 4.1. (a) Bidirectional soft silicone curvature sensor and the measurement setup. (b) Testing objects with different positive/negative bending curvatures up to 80 m^{-1}.

In this study, Ecoflex® GEL from Smooth-On Inc. [62] is adopted as the silicone material. This soft material is elastic and capable of being stretched many times and still rebounds to its original shape without any distortion. In addition, it is certified for biological evaluation of medical devices with irritation and skin sensitization tests. The fabrication process mainly consists of four steps, which are (1) mold design and 3D printing, (2) lower layer molding, (3) FBG integration and upper layer molding, (4) de-molding. In step (1), the mold of silicone rubber is fabricated through a 3D printer with a fabrication precision of 50 μm. Then in step (2), equal amount of Ecoflex solutions are mixed and poured into the mold to fabricate the lower layer of the curvature sensor with a thickness of h_2, as illustrated in Figure 4.2. In step (3), a FBG is placed on the top of the lower layer, leveled, and is fixed at the two end of the FBG, such that it is flat and parallel to the surface of the mold. Then, the mixed silicone solution is poured into the mold to create the upper layer with a thickness of h_1. The silicone rubber is cured for 4 hours at a temperature of 25 °C. Finally, the curvature sensor is demolded after the upper layer is cured. In the test experiment, the overall dimensions of the sensor are 5 mm in height ($h_1 + h_2$), 10 mm in width and 20 mm in length. The FBG used in the sensor is a standard FBG fabricated by UV written technique, which has uniform grating pitches, an overall grating length of 20 mm, side-mode suppression of 26 dB, and a reflectivity of 92.9%. In the test the thicknesses of upper layer (h_1) and lower layer (h_2) are set ranging from 4.5:0.5 to 2.5:2.5 (mm) in five sensor samples, such that the relation between the FBG offset position and sensor sensitivity can be investigated.

4.2.1 Measuring Principle

When the FBG embedded sensor is placed on top of a curved surface, bending occurs on both the silicone sheet and the embedded FBG. Two bending directions, +z and –z, can be observed on a curved surface, that positive bending is defined as when the FBG is closer to the inner arc of the bend, while negative bending is defined when the FBG is further away from the inner arc, as illustrated in Figure. 4.2(b) and 4.2(c). The reflected wavelength λ_B of the FBG is determined by its grating period, which can be written as Eq. (4.1)

$$\lambda_B = 2\, n_e \cdot \Lambda \tag{4.1}$$

where ne and Λ are the effective refractive index and the grating period, respectively. The bending effect of the embedded FBG will either stretch or compress the grating period, resulting in a change in the reflected wavelength. Stretched gratings will have a longer grating period Λ causing the reflection peak λ_B shift to longer wavelengths (red shift), while compressed gratings will result in a shift to shorter wavelengths (blue shift).

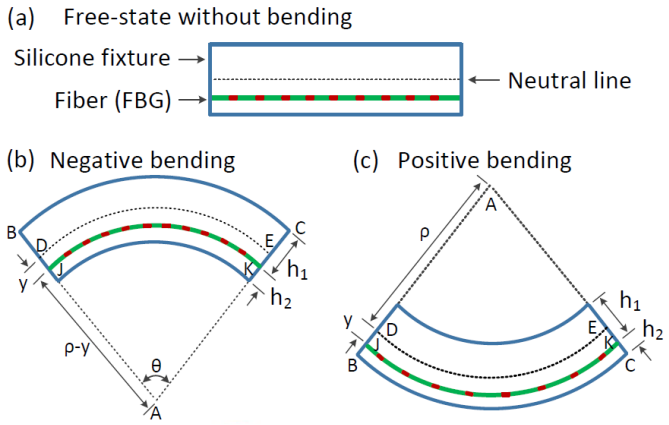

Figure 4.2. Operating principle of the FBG based bidirectional curvature sensor. (a) Free-state of the curvature sensor, the dashed black line is the neutral line of the sensor, green line is referring to the fiber and red dash line is the FBG. (b) Negative bending situation. (c) Positive bending situation.

Different from most of the FBG based curvature sensors where the gratings are glued at the surface of the sensor, the FBG in our approach is embedded at an offset position from the neutral line (indicated by the dashed line *DE* in Figure 4.2(b)). As a result, positive bending and negative bending have different effects on the grating period. The distance from the FBG to the outer arc and inner arc of the silicone sheet is defined as h_1 and h_2, respectively, as shown in Figure 4.2(b) and 4.2(c). The design and analysis of our sensor are based on the pure bending model [63], which is a classic and widely adopted model in mechanical engineering for describing a bending moment. Thus, when the sensor is bent as illustrated in Figure 4.2(b), the relationship between the length of the neutral line, bending radius, and the bending angle is governed by

$$L_{DE} = \rho \cdot \theta \tag{4.2}$$

where L_{DE} is the length of the neutral line of the silicone sheet, which is always a constant value under all curvatures according to pure bending model [17]. ρ and θ are the radius and central angle at the neutral line, respectively. In general, the curvature C and the bending radius has a reciprocal relationship, as

$$C = 1/\rho = \theta/L_{DE} \tag{4.3}$$

Since the FBG is very thin and is embedded inside the silicone sheet, the FBG and the silicone sheet can be treated as a uniform object undergoing the same bending. That is to say, the FBG is compressed during negative bending, while it is stretched during positive bending. The offset location (y) of the FBG results in slightly modification in the bending radius and is represented by $\rho \pm y$, depending on if it is a positive or negative bending. Then, we can obtain the length of FBG (L_{JK}) under an applied curvature, as

$$L_{JK} = (\rho \pm y) \cdot \theta \tag{4.4}$$

$$\Delta L_{FBG} = L_{DE} - L_{JK} = \pm \theta \cdot y \tag{4.5}$$

$$y = h_1-(h_1+h_2)/2 \tag{4.6}$$

where y is the distance between the neutral line and the FBG, and is fixed for a certain design. The bending induced change in the FBG length is derived as Eq. (4.5), which means that the grating period is changed proportionally to the bending angle θ (or curvature C), thus, a wavelength shift of the Bragg wavelength is resulted according to Eq. (4.1) and Eq. (4.3), and can be described as

$$\Delta\lambda_B \propto \pm n_e \cdot C \cdot L_{DE} \cdot (h_1-h_2) \tag{4.7}$$

In Eq. (4.7), L_{DE} is a constant value in the pure bending model, and h_1 and h_2 are predetermined during the fabrication process for each sensor. Consequently, the amount of the wavelength shift is solely governed by the measured curvature C. It is worth noticing that the sensor is designed to be thin and small, and is for measuring relative large curvatures (i.e. $\rho >> y$). However, when the measured curvature is comparable to the sensor thickness, then C should be considered as,

$$C=1/(\rho \pm y) \tag{4.8}$$

and a small measurement difference between positive and negative bending will be resulted. This explains the discrepancy that will be seeing in the measured results in Figure 4.3 when the offset (y) is large.

During the design of the curvature sensor, the value of h_1-h_2 provides the feasibility to adjust the sensor sensitivity as well as the capability to measure bi-direction bending. Showing in Figure 4.2(b) is a situation when the FBG is bent closer to the inner arc, i.e. h_1-h_2 is a negative value (negative bending), a compression of the FBG is obtained because $L_{DE} > L_{JK}$. As a result, a blue shift of the Bragg wavelength is obtained from the reflection spectrum. On the contrary, when the sensor has a positive bending as shown in Figure 4.2(c), i.e. h_1-h_2 is a positive value, stretching of the FBG and a red shift is observed. Finally, by measuring the direction and the amount of the

wavelength shift, both the bending directions and curvatures can be determined. Notice that if the FBG is positioned at the neutral line of the sensor, i.e. h_1 equals h_2, L_{DE} is always a constant under pure bending, meaning that $\Delta\lambda_B$ is always 0. The sensor's sensitivity is governed by the amount of wavelength shift under certain amount of bending, which is determined by the h_1-h_2 value according to Eq. (4.7). Thus, by adjusting the FBG embedded depth during the fabrication process, different sensitivities can be resulted. The measurement setup consists of a broadband light source, an optical circulator, and an optical spectrum analyzer. Two sets of testing objects, a total of 15 pieces (including a flat surface) with 8 different bending curvatures from 0 to 80 m^{-1} are used. The concave (red) and convex (black) testing objects are used for negative and positive bending measurement respectively.

4.2.3 Results and discussion

Figure 4.3 shows the measured reflection spectra of the proposed FBG embedded silicone curvature sensor in response to different bending curvatures. The tested sensor has a 20 mm FBG inside, with embedded h_1:h_2 values of 4:1 (mm). The sensor is put on the top of the testing objects with bending curvatures from 0 to 80 m^{-1} as shown in Figure 4.1(b). Measured spectra resulting from negative bending and positive bending are shown in Figure 4.3(a) and 4.3(b), respectively. As shown in the negative bending situation in Figure 4.2(a), FBG reflection peak gradually shifts to the shorter wavelength direction as the curvature increases, with a total wavelength shift of 0.091 nm under a curvature of 80 m^{-1}. During positive bending situation, the peak shifts to the longer wavelength direction, with a total wavelength shift of 0.095 nm under the same curvature. The measurement sensitivity is 1.1375 pm/m^{-1} for negative bending and 1.1875 pm/m^{-1} for positive bending.

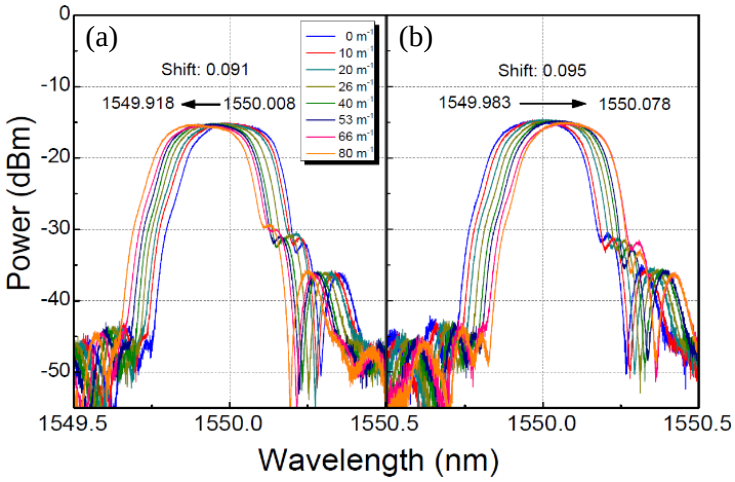

Figure 4.3. Measured FBG reflection spectra of the curvature sensor under different bending curvatures, with embedded h_1:h_2 values of 4:1 (mm). (a) Negative bending. (b) Positive bending.

The experiment agrees with the theoretical predictions that the direction of the wavelength shift in response to positive bending and negative bending are opposite, and can be used to distinguish the bending directions. The profile of the FBG reflection peaks, as well as the property of the silicone material, are well maintained throughout the bending from 0 to ±80 m^{-1}. A further increase in measured curvature to above ±80 m^{-1} will cause over bending of the sensor and unequal changes in grating period, which will result in chirping of the FBG as well as potential damage of the sensor. The response of the sensor is instantaneous and can measure dynamic movements in real-time without the need of molding/formation process. Due to the small amount of wavelength shift, a large number of FBG sensors at different wavelength can be cascaded in a single fiber for multi-point curvature sensing or shape sensing.

We also studied the relationship between the sensor sensitivity and FBG embedded depth by fabricating four testing sensors with different embedded depths (h_2) from 0.5 mm to 2.0 mm. Figure 4.4(a) shows the measured FBG reflection peak shifts of the four sensors under both positive and negative bending curvatures from 0 to 80 m^{-1}. Four identical FBGs are used, with the

same reflection wavelength, initial grating period, grating length (20 mm) and overall sensor size. The h_1:h_2 values for the #1 to #4 sensors are 4.5:0.5, 4:1, 3.5:1.5 and 3:2 (mm), respectively. As shown, positive bending results of all the four sensors show blue wavelength shifts, corresponds to compressions in grating period; while negative bending results in red wavelength shifts, indicating stretching in grating period. Under the same amount of bending curvature, the amount of wavelength shift is governed by the FBG embedded depth, i.e. h_1-h_2 value, which in turn governs the sensitivity. Figure 4.4(b) shows the calculated sensitivities of the four FBG sensor samples with different embedded depths. As shown, similar sensitivities of positive and negative bending are recorded at the same h_1-h_2 values, and the sensor sensitivities increase as the h_1-h_2 values increase. A largest bending sensitivity of 1.64 pm/m^{-1} is achieved with an embedded depth of 0.5 mm. All the measurements are repeated five times and corresponding error bars are shown in Figure 4.4(a) to indicate the variances. The sensors have good accuracy and consistency over different measurements. A control experiment is also performed that a same FBG is embedded at the neutral line of the silicone sheet, with $h_1 = h_2$, while all the fabrication and experiment parameters are set to be the same as before. In this test, there is no significant wavelength shift for both positive and negative bending. This particular structure is incapable to tell the direction of bending, since the compression or stretching of the gratings are not significant when bending is applied, as predicted in the pure bending model in Eq. (4.7). It is worth noticing that to properly protect and fix the FBG inside the silicone sheet for measuring large bending curvatures, a minimum protection thickness of 0.5 mm between the FBG and the sensor surface is needed.

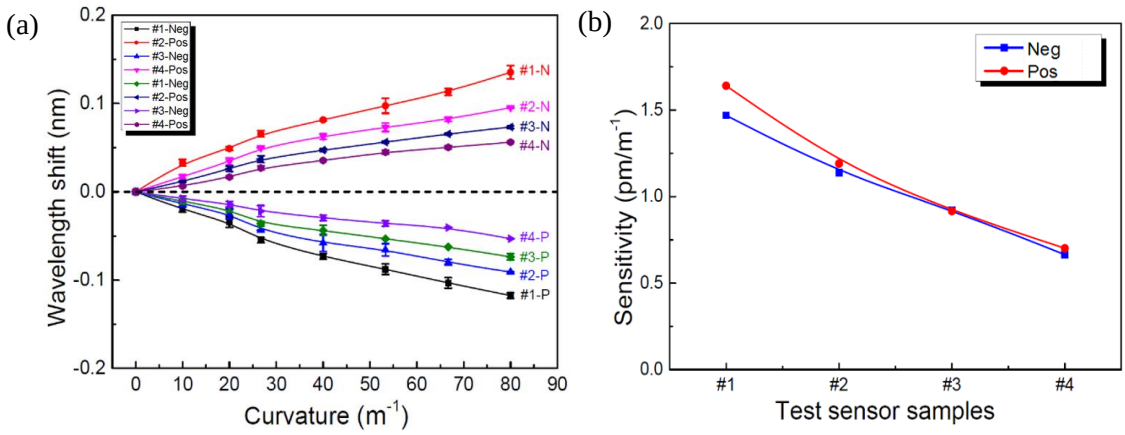

Figure 4.4. (a) Measured reflection peak shifts of 4 tested sensors under different amount of curvatures, with different FBG embedded depths. h_1:h_2 values for #1 to #4 sensors are 4.5:0.5, 4:1, 3.5:1.5 and 3:2 (mm), respectively. (b) Comparison of the sensor sensitivities with different FBG embedded depths, for both positive and negative bending.

4.2.4 Summary

A bidirectional soft curvature sensor based on embedding a FBG in a flexible silicone sheet is demonstrated. Unlike conventional FBG curvature sensor, the proposed sensor has the FBG being embedded offset from the neutral line of the silicone sheet without using any adhesives. The soft silicone sensor does not require a formation time during measurement, enabling real-time curvature sensing. A large curvature measurement range of 80 m-1 is obtained for both positive and negative bending. The relationship between FBG embedded depth and sensor sensitivity is studied through the pure bending model and verified experimentally. The amount of wavelength shift has a linear relationship with the bending curvature for various embedded depths. A design with multiple FBGs is anticipated for sensing shapes with rather complex morphology. Such continuous FBG-based sensing technique makes it possible to acquire high-fidelity geometric details of many non-rigid objects deformed by the dynamic and unstructured environment, in

particular for real-time structural monitoring in civil engineering, robotic control in mechanical engineering, and in vivo procedure in biomedical applications.

4.3 Three-dimensional Shape Sensor

As such, the following work is drawn from our paper published on Optics Express (vol. 25, pp. 24727-24734, Oct. 2017) by Li Xu, Jia Ge, Jay H Patel, and Mable P. Fok entitled "Dual-layer orthogonal fiber Bragg grating mesh based soft sensor for 3-dimensional shape sensing".

With the help of the bi-directional curvature sensor developed in the previous section, we demonstrated a compact soft 3D shape sensor that can measure the complete 3D shape of an object surface. The sensor consists of 18 standard FBGs curvature sensors developed before, and utilizing a dual-layer orthogonal FBG mesh structure to achieve the bi-directional 3D shape sensing. The 18 FBGs are aligned orthogonally in a dual-layer mesh structure with 9 FBGs in the x-direction at the top layer and 9 FBGs in the y-direction at the bottom layer. Embedding the FBGs in two layers enables the sensing of both convex and concave object surfaces, while the two orthogonal layers decompose a curved surface into two orthogonal axes. The FBGs are embedded in and protected by the soft silicone rubber, allowing the FBGs to be bend along the bending curvature of the measured object due to the flexible property of silicone. The proposed scheme can measure the complete 3D shape of an object surface simply by placing the sensor on top of the object. The measured results are plotted out in a 3D visual figure, which provides good intuition of the 3D shape of the measured object. The compact and soft silicone rubber is highly compatible with human body, making the proposed sensor a promising design for wearable monitoring devices and medical robotics.

4.3.1 Design and Fabrication

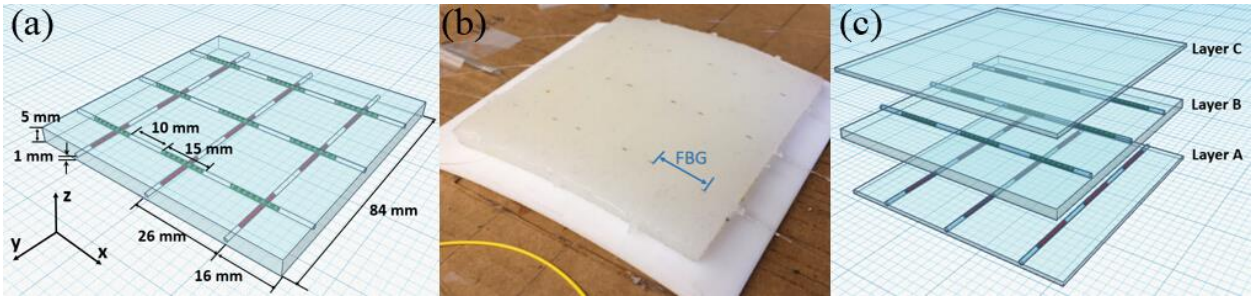

Figure 4.5. (a) Schematic diagram of the proposed 3D shape sensor based on dual-layer orthogonal FBG mesh. Green gratings: FBGs at the top layer; Red gratings: FBGs at the bottom layer. (b) Prototype of the fabricated soft 3D shape sensor. (c) Illustration of different layers of the silicone sheet and the dual-layer orthogonal FBG mesh structure.

The 3D shape sensor is composited of 18 FBGs and a silicone sheet of 84 mm × 84 mm in size and 5 mm in thickness. 18 FBGs with different center wavelengths are embedded in the silicone sheet, resulting in 18 sensing points in two orthogonal directions. The FBGs are embedded in two off-center layers (red and green) that enables the measurement of shape change in both concave (-*z*) and convex (+*z*) directions. The top layer FBGs (green) are embedded 1 mm below the top surface, while the bottom layer FBGs (red) are embedded 4 mm below the top surface (i.e. 1 mm above the bottom surface). According to the study in previous section, 1-mm silicone sheet outside the fiber can provide enough protection to the FBGs while enabling good sensitivity at the same time. The top and bottom layers each has 9 FBGs embedded orthogonally in *x*- and *y*-directions, such that the curvature information of an object surface can be decomposed into two orthogonal axes. The *x*-direction FBGs (green) are arranged into three rows, while the *y*-direction FBGs (red) are arranged into three columns. Each FBG is 15 mm long and is placed with a 10-mm gap between adjacent FBG. The distance between adjacent row/column is 26 mm and is 16 mm

from the edge of the silicone sheet. All the FBGs are written on the same fiber, enabling one single measurement for capturing information from all the 18 FBGs. The design of the proposed soft 3D shape sensor is shown in Figure 4.5.

To fabricate the sensor, Ecoflex® 00-10 from Smooth-On Inc. is used as the silicone material, which is flexible, ductile, and can be recovered to the original shape after many times of measurement, such that a good repeatability is obtained for the shape measurement. The silicone material has tensile strength of 120 psi, maximum elongation of 800%, shrinkage of <0.001 in./in, and operating temperature from -65 °F to 450 °F. Furthermore, the silicone material is very soft and can be attached on top of the measured object with same shape. Three molds that are used for precisely controlling the FBG embedded thickness and holding the FBGs in place are first designed and fabricated through 3D printing. Two of the molds (mold 1 and mold 2) are used to make Layer A and Layer B in Figure 4.5(c) with thicknesses of 1 mm and 3 mm, respectively. The third mold (mold 3) is used as the final assembling mold, which has a total thickness of 5 mm and has precise v-grooves on each of the sidewalls to fix the optical fiber at the right position. First, Layer A and Layer B are made by mixing equal amount of Ecoflex® 00-10 solutions A and B, and let it cure for 4 hours in mold 1 and mold 2. Layer A is then transferred to mold 3 for reassembling of the shape sensor. An optical fiber with the first set of FBGs (a total of 9 FBGs) is put on top of Layer A and are arranged in 3 rows, where the exact position of the fiber is precisely fixed by the v-grooves on the sidewalls of mold 3. Layer B is then transferred from mold 2 to mold 3 and is put on the top of the fiber above Layer A. Small amount of silicone mixture is added between Layer A and Layer B to ensure the two layers are securely assembled together. Next, another optical fiber with the second set of FBGs is put on top of Layer B in the direction that is orthogonal to the first set. At last, mixed silicone solution is poured into mold 3 to form Layer C after the FBGs are

secured at the v-grooves, which are cured together with the rest of the shape sensor in 4 hours. Finally, the two pieces of optical fiber that consists of the orthogonally arranged FBGs are cascaded externally through fusion splicing, such that it becomes a single piece of fiber with all the 18 FBGs on it. A photo of the fabricated soft shape sensor is shown in Figure 4.5(b). The unique orthogonal dual-layer structure enables the sensor to measure shape changes in both bending directions – positive bending (convex) and negative bending (concave), as well as decomposing each bending in two orthogonal directions. It is worth to mention that unlike most FBG based designs that use special glues to fix the FBG onto the sensors fixture which will affect the property of the FBG - our approach does not require any adhesive, resulting in full utilization of the FBG property and a wide measurement range.

4.3.2 Measuring Principle

As demonstrated in the previous section, each sensing point (FBG) of the 3D shaper sensor works as a curvature sensor at a particular position, the relationship between the bend radius and length of neutral line can be governed by

$$\rho = Ln/\theta \tag{4.9}$$

where Ln is the length of neutral line, ρ is the bend radius and θ is the central angle. When the FBG curvature sensor is placed on the surface of an object with a positive bending curvature, stresses and strains are negative above the neutral plane, but they are positive below the neutral plane. Thus, the FBG that is fixed at the top layer will be stretched while the FBGs fixed in the bottom layer will be compressed, essentially changing the FBG Bragg wavelength λ_B. Therefore, taking an example of FBGs fixed in top layer, negative bending curvature (Figure 4.6(a)) results

in a Bragg wavelength λ_B shifts to the longer wavelength (right), while positive bending curvature (Figure 4.6(b)) results in a shift to the shorter wavelength (left) [17].

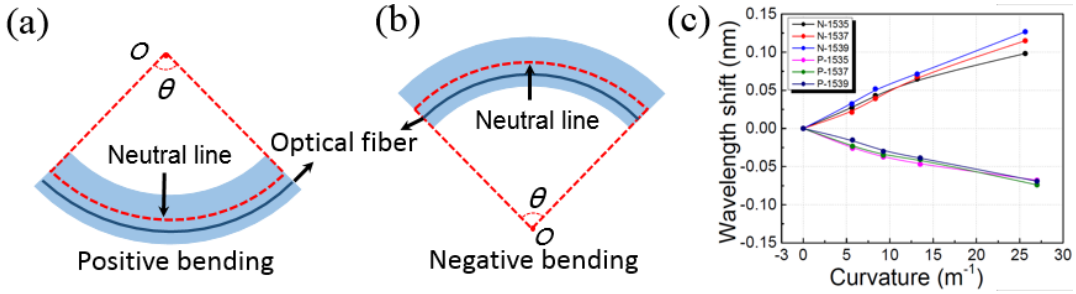

Figure 4.6. Measurement mechanism of each of the sensing point working as a curvature sensor, when measuring an object with a (a) negative bending curvature and (b) positive bending curvature. (c) Wavelength shifts in response to different bending curvatures for both positive and negative bending directions.

Since each FBG is considered as a curvature sensor at a particular position inside the 3D shaper sensor, by measuring the amount and direction of the wavelength shifts of all the 18 FBGs in both layers, both bending curvatures and directions can be obtained at each sensing points, thus 3D shape reconstruction of the measured object can be achieved.

A broadband light source (S5FC1005S Fiber Coupled Super Luminescent Diode from Thorlabs Inc.) with wavelength range from 1290 nm to 1660 nm is used as the light source. An optical circulator is used to couple the light into the optical fiber that has all the 18 FBGs written on it. Since all the FBGs are cascaded inside the same fiber and with different reflection peaks, only one light source is enough for all the 18 sensing points. Light at each Bragg wavelength is reflected back from each sensing point and is then launched into an optical spectrum analyzer (OSA) (APEX AP2040A) via port 3 of the same optical circulator. The OSA has a resolution of 0.8 pm to measure the reflected optical spectra of the FBGs. Spectrum with 18 different Bragg

wavelength peaks can be obtained by one measurement, which includes the measured results from all the 18 sensing points.

4.3.3 Calibration

First, we calibrate the relationship between shifts in λ_B and the bending curvature of each FBG. The wavelength shift is measured by placing the 3D shape sensor on eight cylindrical reference objects with different but known curvatures. The bending curvature C is expressed in terms of bending radius ρ as $C=1/\rho$. We use cylindrical objects with negative curvatures of 5.62 m^{-1}, 8.33 m^{-1}, 13.16 m^{-1}, and 25.64 m^{-1} and positive bending curvatures of 5.69 m^{-1}, 9.25 m^{-1}, 13.51 m^{-1}, and 27.02 m^{-1} for calibration.

By repeating the curvature measurement at all the 18 sensing points with reference objects, we can get five calibration points for each sensing point. Linear fitted lines are used to connect the calibration points and the resultant calibration curves are resulted. As an example, calibration curves of three FBGs in the same row (Bragg wavelengths at 1535 nm, 1537 nm and 1539 nm) are shown in Figure 4.6(c) shows. The Bragg wavelength shift and the bending curvature have a linear relationship for both positive and negative bending directions, which is studied in our previous work [17]. Sensitivity of negative and positive bending directions for these FBGs are around 3.8 pm/m^{-1} and -2.5 pm/m^{-1}, respectively. With the calibration curves, the actual bending curvatures of an unknown object can be calculated by fitting the Bragg wavelength shift to the calibration curves. The sensitivity of each sensing point varies slightly from each other due to the slight difference between different FBGs fabrication process and the FBG embedded depth in the sensor. Therefore, calibration curves for all the 18 FBGs under both positive and negative bending are measured. Thus, in the 3D shape measurement, by using the slopes (S) of the fitted lines, bending

curvatures for the 18 sensing points can be calculated from the measured wavelength shift ($\Delta\lambda$) through the relationship $C=\Delta\lambda/S$.

4.3.4 3D Shape measurement and reconstruction

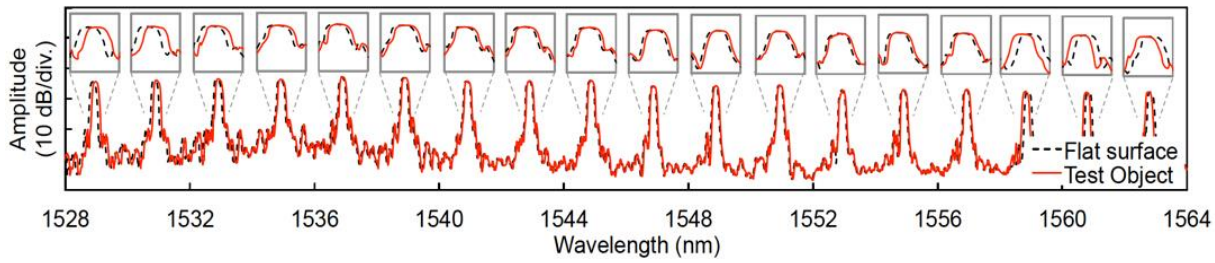

Figure 4.7. Optical spectra of the 18 FBG sensing wavelengths. Insets: zoom in view of each FBG reflection peak.

To measure the shape of an object, the soft sensor is placed on the surface of a test object to measure the wavelength shift at each sensing point. Due to the irregular shape of the test object, the amount of Bragg wavelength shift and the shifting direction in each FBG are different (as shown in the zoom in insets) – which corresponds to the bending curvature and bending direction at each of the sensing point, respectively. Figure 4.7 shows the measured optical spectra of all the 18 FBGs inside the shape sensor for a 3D object. The black curve is the initial spectrum when the shape sensor is put on a flat surface, while the red curve is the measured spectrum when the sensor is put on a non-flat object of interest. Then, bending direction at certain sensing point can be measured based on the wavelength shift direction at the corresponding Bragg wavelength, while the bending curvature can be calculated through the relationship between wavelength shift and the calibration curve slope using equation $C=\Delta\lambda/S$.

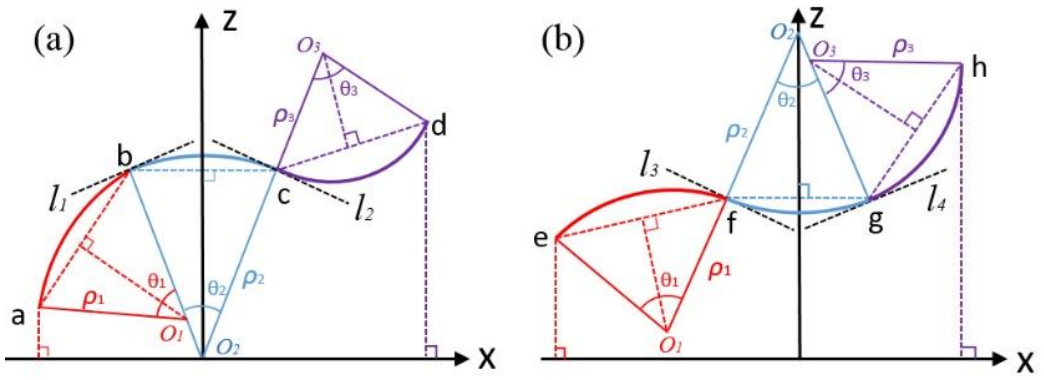

Figure 4.8. Examples of changes in curvature at the shape sensor. Each section - *ab*, *bc*, and *cd* correspond to each FBG sensor arc.

The contour of the object along the row/column can be approximately reconstructed by connecting the measured curvature of the three arcs. Furthermore, adjacent arcs share the same tangent line, e.g. arcs *ab* and *bc* share the tangent line *l1*. 3D coordinates of all the 18 sensing points can be calculated through the following steps:

1. Curvature information is obtained through the spectral measurement and calibration curves. Then, bending radiuses of each sensing points is calculated using $\rho = 1/C$.
2. The bending angles θ_1-θ_3 can be calculated using the relationship $\theta_n = arc\ length/\rho n$. According to Figure 1(a), arc lengths of *ab* = 29.5 mm, *bc* = 25 mm, and *cd* = 29.5 mm.
3. Circle centers of the arcs are O1 (*x1*, *z1*), O2 (*x2*, *z2*) and O3 (*x3*, *z3*), while the bending radiuses are ρ_1, ρ_2, ρ_3, respectively.
4. Let's use Figure 4.8(a) as an example, assume O_2 is at (0, 0), (*x*, *z*) coordinates of O_1 and O_3 can be calculated as:

$$x_1 = -(\rho_2 - \rho_1)\sin\frac{\theta_2}{2}, \qquad z_1 = (\rho_2 - \rho_1)\cos\frac{\theta_2}{2}. \tag{4.10}$$

$$x_3 = (\rho_2 + \rho_3)\sin\frac{\theta_2}{2},$$
$$z_3 = (\rho_2 + \rho_3)\cos\frac{\theta_2}{2}. \tag{4.11}$$

5. The coordinates of the each ends of the arcs, i.e. point *a*, *b*, *c*, *d*, can then be calculated by:

$$x_a = -(2\rho_1 \sin\frac{\theta_1}{2}\cos(\frac{\theta_1}{2} + \frac{\theta_2}{2}) + \rho_2 \sin\frac{\theta_2}{2}),$$
$$z_a = \rho_2 \cos\frac{\theta_2}{2} - 2\rho_1 \sin\frac{\theta_1}{2}\sin(\frac{\theta_1}{2} + \frac{\theta_2}{2}). \tag{4.12}$$

$$x_b = -\sin\frac{\theta_2}{2}\rho_2,$$
$$z_b = \cos\frac{\theta_2}{2}\rho_2. \tag{4.13}$$

$$x_c = \sin\frac{\theta_2}{2}\rho_2,$$
$$z_c = \cos\frac{\theta_2}{2}\rho_2. \tag{4.14}$$

$$x_d = \rho_2 \sin\frac{\theta_2}{2} + 2\rho_3 \sin\frac{\theta_3}{2}\cos(\frac{\theta_3}{2} - \frac{\theta_2}{2}),$$
$$z_d = \rho_2 \cos\frac{\theta_2}{2} + 2\rho_3 \sin\frac{\theta_3}{2}\sin(\frac{\theta_3}{2} - \frac{\theta_2}{2}). \tag{4.15}$$

6. Functions of arcs *ab*, *bc*, and *cd* can then be formulated as follows:

$$z_{ab} = \sqrt{\rho_1^2 - (x + (\rho_2 - \rho_1)\sin\frac{\theta_2}{2})^2} + (\rho_2 - \rho_1)\cos\frac{\theta_2}{2}, (x_a < x < x_b, z_a < z_{ab} < z_b). \tag{4.16}$$

$$z_{bc} = \sqrt{\rho_2^2 - x^2}, (x_b < x < x_c, z_b < z_{bc} < z_c). \tag{4.17}$$

$$z_{cd} = \sqrt{\rho_3^2 - (x - (\rho_2 + \rho_3)\sin\frac{\theta_2}{2})^2} + (\rho_2 + \rho_3)\cos\frac{\theta_2}{2}, (x_c < x < x_d, z_c < z_{cd} < z_d). \tag{4.18}$$

7. Similar mathematics relationship can be found to represent another curve situation shown in Figure 4.8(b). Coordinates of all the arcs are obtained and incorporated in a single plot for 3D reconstruction in MATLAB.

The MATLAB code based on the previous 3D reconstruction algorithm is included in the APPENDICE B. To test the performance of the 3D shape measurement and the reconstruction capability of the MATLAB program, three test objects of different shapes are used, including a half cylindrical surface, a hemisphere, and an irregular shape object, as shown in Figure 4.9(a)-4.9(c), respectively. The soft shape sensor is placed on top of the test object and the optical spectrum of the whole FBG mesh is measured. 3D shapes of the test objects are reconstructed as shown in Figure 4.9(d)-4.9(f). Surface shapes of the test objects are well reconstructed with accurate matching profiles. It is worth noticing that due to the bending limitation of FBGs and the tension limitation of the silicone gel material, the shape sensor has a bending curvature limit of 25.64 m^{-1}. Measurement of objects with curvature larger than the curvature limit will results in large measurement error. The spatial resolution of the shape sensor is 26 mm which is governed by the density of FBGs in the dual-layer FBG mesh, which can be increased by using shorter FBG and closer spacing between each FBG in the mesh.

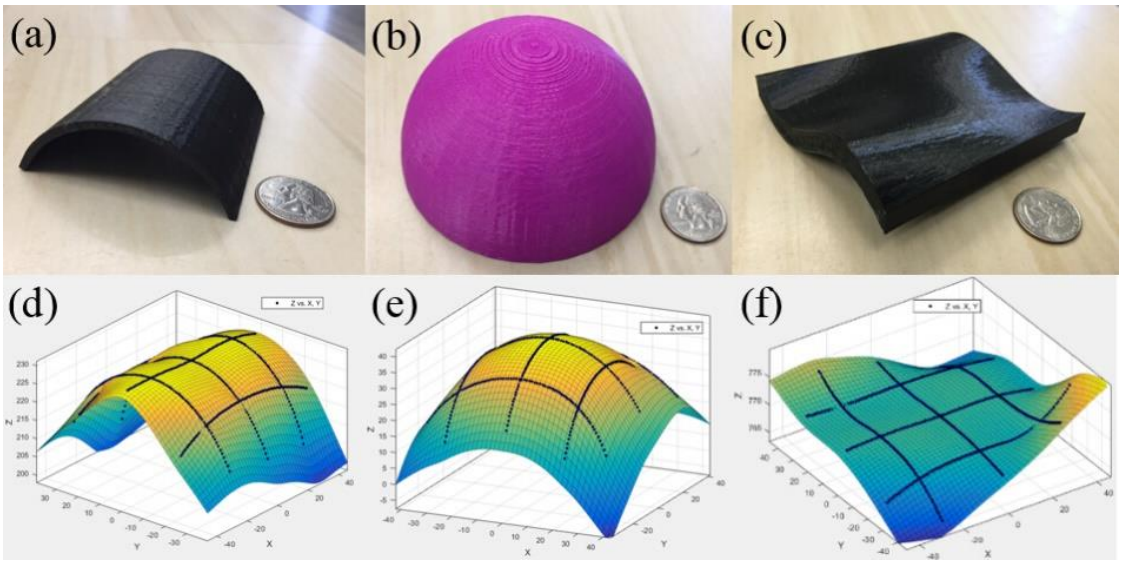

Figure 4.9. (a)-(c) Testing objects #1 to #3; (d)-(f) Reconstructed 3D shapes of the corresponding testing objects.

The accuracy of shape sensor is tested using reference cylindrical objects with various bending radius ρ which are known before measurement. The measurement error is about 2.7% calculated by the error formula shown in Eq. (4.19)

$$\%E=|(\rho_a-\rho_e)/\rho_a\ |\times 100 \tag{4.19}$$

where ρ_a represents the actual bending radius and ρ_e represents the measured bending radius. This small measurement error provides a good visual idea of the 3D shape under testing. Although the silicone material provides short-term temperature isolation, we are aware that just like other FBG sensors, our approach is sensitive to temperature. To compensate the temperature effect, a reference FBG can be placed at the center layer (neutral line) of the silicone sheet. Based on pure bending model, the reference FBG will not be affected by bending and could acts as a reference for decorrelating the temperature effect.

4.3.5 Summary

In this section, a soft silicone shape sensor for 3D shape measurement is designed and experimentally demonstrated, with 18 FBGs embedded in a flexible silicone rubber. The 18 FBGs are located in two orthogonal layers – resulting in a dual-layer orthogonal mesh structure and 18 sensing points. The dual-layer structure enables the measurement of both positive and negative bending curvatures, while the orthogonal structure decompose a curve into *x*- and *y*- axis. The bending direction and bending curvature at each sensing point are obtained by measuring the direction and amount of Bragg wavelength shift of each FBG in the mesh. The surface profiles of the test objects are successfully reconstructed with visual 3D plotting. The reconstructed results show good accuracy and visualization of the test object. This compact and flexible design makes the proposed 3D shape sensor a good candidate for wearable devices, soft robotics and biomedical applications.

4.4 Stretchable Sensor for Strain, Torsion and Curvature Measurement

As such, the following work is drawn from our submitted manuscript for OFC on 10/10/2017 by Li Xu, Ning Liu, Jia Ge, Xianqiao Wang and Mable P. Fok entitled “Stretchable multi-function fiber sensor for tension, bending and torsion sensing”.

In this section, we develop a soft stretchable multifunction sensor based on the use of an FBG, which is embedded as a sinusoidal structure in a silicone sheet at an off-center position. This unique sinusoidal structure and the flexibility of silicone sheet make the sensor highly stretchable, while embedding the FBG at an off-center position enables the sensing for bi-directional bending curvatures and torsion directions during twisting. Unlike most proposed sensors which can only detect deformation or measure single variable parameter, the proposed stretchable sensor can

achieve accurate measurement for strain, torsion direction, and bending curvature. The stretching ability, flexibility, and compact structure of the demonstrated fiber optic sensor is highly desired in biomedical applications and soft robotics which is compatible with human body and can be mount onto a flexible object that has large movement during measurement.

4.4.1 Principle and experimental setup

Figure 4.10(a) and 4.10(b) shows the design and photo of the soft stretchable fiber optic sensor, respectively, that consists of a silicone sheet and a FBG. The size of the silicone sheet is 60 mm × 60 mm with a 4-mm thickness. A 15-mm long FBG is located in the middle of a sinusoidally-placed optical fiber that is embedded in an off-centered layer in the silicone sheet with a 3mm embedded depth from the top and 1 mm from the bottom. A 3D printed mold with 60 mm × 60 mm in size and 4-mm depth is used to fabricate the stretchable sensor. Small columns are fixed in the mold to fix the optical fiber in a sinusoidal shape. Small notches on the mold's sidewalls are used to support the optical fiber at the desired embedded depth. Then, equal amount of Ecoflex® 00-10 solutions A and B are mixed uniformly to form the silicone mixture and poured into the mold. The silicone mixture is cured in 4 hours and the stretchable FBG sensor is made. Although the silicon glass material of the optical fiber itself is not stretchable, the sinusoidal structure enables the FBG written optical fiber to be stretched with the silicone sheet without breaking, only a deformation in the sinusoidal shape is resulted.

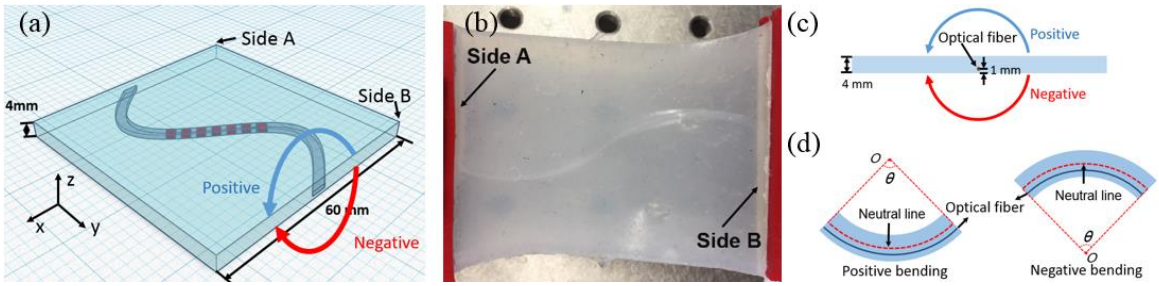

Figure 4.10. (a) Design of the proposed stretchable sensor based on a sinusoidal-structured FBG embedded at an off-center position in a silicone sheet. (b) Cross section of the stretchable sensor from side B showing the positive and negative torsion directions. (c) Photo of the stretchable sensor prototype under stretching. (d) Measurement mechanism of the stretchable sensor when measuring an object with positive and negative bending directions.

With the unique structure, the proposed stretchable fiber optic sensor is capable of measuring strain, bidirectional curvature, and torsion direction. When the proposed sensor is stretched, the sensor is elongated in the y direction, which in turn changes the strain of the silicone and FBG. Therefore, strain applied to the sensor will result in a shift of FBG Bragg wavelength, governed by $\Delta\lambda_B = [(1 - p_e)\varepsilon + (\alpha_\Lambda + \alpha_n)\Delta T]\ \lambda_B$ (Eq. (4.20)), where $\Delta\lambda$ is the resultant wavelength shift, λ_B is the initial Bragg wavelength without strain, p_e is photoelastic coefficient, ε is the strain applied to the FBG, α_Λ is the thermal expansion coefficient, α_n is the thermos-optic coefficient and ΔT is temperature change. Gage factor $k = (1 - p_e)$ is calculated to be 0.78 and temperature is kept constant during the measurement. According to Eq. (4.20), the resultant Bragg wavelength shift $\Delta\lambda$ has a linear relationship with the applied strain ε, thus, the strain can be obtained by measuring the Bragg wavelength shift using an optical spectrum analyzer and calculate using Eq. (4.20).

Another parameter the proposed sensor can measure is the curvature and direction of a bending. Although bending curvature can be easily measured with most fiber optic sensors, the measurement of bending direction is unique to our approach, which is enabled by embedding the

FBG at an off-center position in the *z* axis. According to our previous study [17], when the FBG is embedded off-center, i.e. below the neutral line of the silicone sheet, the FBG is stretched when the sensor is put on an object with a positive curvature (concave), resulting in a right shift in the FBG Bragg wavelength. On the other hand, the FBG will be compressed if the sensor is put on an object with a negative curvature (convex), resulting in a left shift in the FBG Bragg wavelength. This observation can be explained by the pure bending model in mechanical engineering. Thus, bending curvatures and bending directions can be measured from the amount of Bragg wavelength shift and the direction of the shift, respectively.

The third parameter that the stretchable fiber optic sensor can measure is torsion direction. Since the FBG is embedded at an off-center position, the FBG is compressed when the sensor has a positive torsion (as shown in Figure 4.10(a)), resulting in a left shift in the FBG Bragg wavelength. On the other hand, the FBG is stretched when the sensor has a negative torsion, resulting in a right shift in the FBG Bragg wavelength.

In our experiment, a broadband light source with wavelength range from 1290 nm to 1660 nm is launched into the FBG via an optical circulator as the input light. The embedded FBG is 1.4 cm long and has a Bragg wavelength at 1550nm. The FBG Bragg wavelength is measured by an OSA with a resolution of 0.8 pm. By analyzing the direction and the amount of Bragg wavelength shift in the FBG, strain, curvature, and torsion direction can be measured.

4.4.2 Results and discussion

To measure the relationship between Bragg wavelength shift and tension applied to the stretchable sensor, we fix one side of sensor on side A (shown in Figure 4.10(b)) and apply force on side B using a pulley and different weights from 60 g to 218 g corresponding to gravity from

0.59 N to 2.14 N. The measured optical spectra of the FBG is shown in Figure 4.11(a), that shows a total of 0.518 nm shift in Bragg wavelength when the applied tension force increases from 0 N to 2.14 N. The relationship between wavelength shift and applied tension force is shown in Figure 4.11(b). A linear relationship is observed with small error bars and sensitivity is 0.25 nm/N. Since the FBG optical fiber is embedded in silicone sheet with a sinusoidal structure, the FBG embedded sensor can be stretched and elongated by 30% when a tension force of 2 N is applied. This unique structure enables fiber optics and FBG to be used in a stretchable sensor for the first time with good stretching ability.

Next, the proposed sensor is tested for its bi-direction curvature sensing capability. As the FBG is embedded at an off-center position in the z-axis, positive bending and negative bending of the sensor will result in stretching and compression of the FBG, respectively. Since the silicone material is soft and flexible, it can easily fit and bend alone a curved object surface. The bending curvature C is expressed in terms of the bending radius R, such that $C=1/R$. Ten cylindrical objects with positive curvatures of 5.62 m^{-1}, 8.33 m^{-1}, 13.16 m^{-1}, 25.64 m^{-1}, 40m^{-1} and negative bending curvatures of 5.69 m^{-1}, 9.25 m^{-1}, 13.51 m^{-1}, 27.02 m^{-1}, 43.48 m^{-1} are used to study and calibrate the relationship between Bragg wavelength shifts and bending curvature. Both positive and negative bending results are shown in Figure 4.12(a), which a linear relationship between Bragg wavelength shift and bending curvature for both bending directions is observed. Sensitivity of 2.3 pm/m^{-1} and 0.49 pm/m^{-1} are resulted for positive and negative bending, respectively.

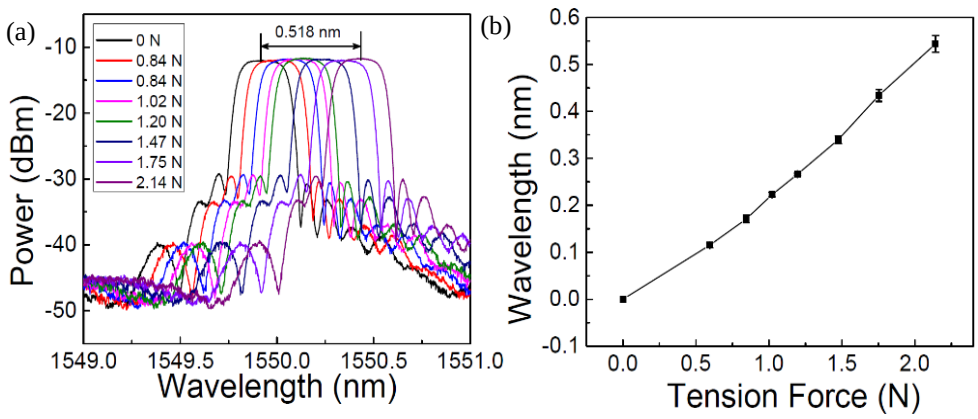

Figure 4.11. (a) Measured spectra of the FBG with different tension forces. (b) The wavelength shifts with different applied tension force from 0 N to 2.14 N.

Lastly, we study the relationship between Bragg wavelength shift and torsion direction in the stretchable sensor. Side A of the sensor is fixed while side B of the sensor is twisted to different directions and angles. Positive and negative twisting directions are defined as side B is twisted anticlockwise and clockwise as illustrated in Figure 4.10(a). As shown in Figure 4.12(b), when side B is twisted anticlockwise, the FBG is stretched and an increase in Bragg wavelength is resulted; on the other hand, when side A is twisted clockwise, the FBG is compressed and a decrease in Bragg wavelength is observed. The larger the twisting angle, the larger the wavelength shift is resulted. Temperature insensitive measurement can be obtained by embedding a reference FBG at the neutral line of the silicone sheet (non-off center position) to decorrelate the temperature effect.

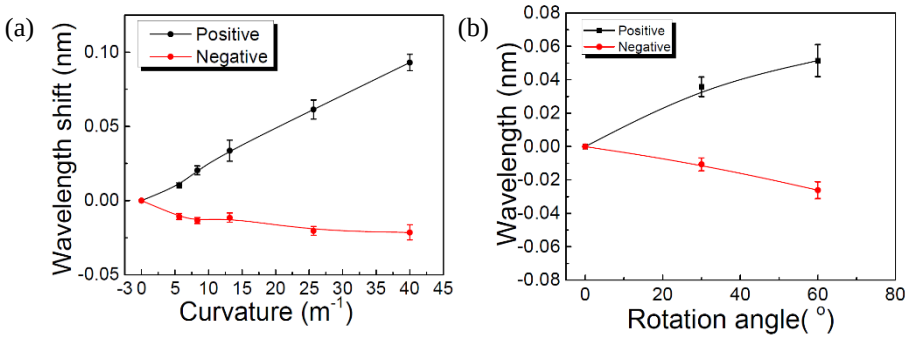

Figure 4.12. (a) Measured wavelength shifts in response of different bending curvatures for both positive and negative bending directions. (b) Measured wavelength shifts in response of different rotation angles for both positive and negative twisting directions.

4.4.3 Summary

A stretchable fiber optic sensor for strain, curvature and torsion direction measurement is proposed and experimentally demonstrated. An optical fiber with FBG is embedded in a sinusoidal structure at an off-center position in a silicone sheet. The sinusoidal structure enables a 30% elongation of the stretchable fiber optic sensor, which cannot be achieved in conventional fiber optic sensors. Furthermore, the off-center embedded position facilitates the extraction of direction information in both curvature measurement and torsion sensing. Measurement of strain, bending curvature, and torsion direction are successfully measured using the stretchable fiber optic sensor. The soft and stretchable sensor is an excellent candidate for sensing in biomedical and soft robotic applications.

4.5 Summary

In this chapter, we demonstrate two FBG based soft sensors for curvature sensing and 3 dimensional shape sensing. In addition, a stretchable fiber optic sensor for strain, curvature and torsion direction measurement is proposed and experimentally demonstrated. The principle for a

silicone sheet based sensor using pure bending model for curvature sensing is introduced. The bidirectional soft curvature sensor is proved having good sensitivity for bending curvature measurement. Furthermore, shape sensing based on 18 curvature sensors and an orthogonal dual layers structure is accomplished and the 3D shape measured by the shape sensor is successfully reconstructed. The sinusoidal structure based stretchable sensor uniquely enables 130% of stretching and facilitates strain, torsion direction and curvature measurement. The soft curvature/ shape sensors and the stretchable sensors are great candidate for wearable devices, biomedical devices and soft robotic applications.

CHAPTER 5
CONCLUSIONS

In this study, several FBG based sensors for contact force measurement and shape measurement are proposed and experimentally demonstrated. In contact force sensor approach for cardiac ablation catheters, we develop a temperature insensitive contact force sensor for mono-directional catheters, which measuring contact force through total reflection power and a temperature and deflection angle insensitive contact force sensor for bi-directional steerable catheters. A spiral structure FBG based sensor is also studied providing a directly contact force measurement method through optical power measuring. In addition, the temperature sensitivities of the all the proposed sensors are studied. Temperature insensitive designs or temperature compensating schemes in normal operating conditions are incorporated to the proposed sensing schemes, making them capable of working under different temperature conditions, which is highly desired in many minimally applications.

Three FBG based soft sensors with different structures for multi-dimensional curve sensing are demonstrated in our study. A bidirectional soft curvature sensor based on off-centered embedded FBG with a flexible silicone sheet is demonstrated, which has the ability to measure bidirectional bending curvatures. Based on this basic structure, a soft 3D shape sensor with 18 FBGs embedded orthogonally in two layers is designed and experimentally demonstrated. Bending directions and curvatures for 18 sensing points are measured and constructed to a 3D shape of test object. Furthermore, an approach to adapt to the requirement for stretching is demonstrated. An FBG is embedded in a sinusoidal structure at an off-center position in a silicone sheet enables as

much as 30% elongation of the stretchable sensor and have ability for strain, curvature and torsion direction measurement. Above soft sensors are excellent candidate for biomedical and soft robotic applications due to the flexibility or stretchable features.

Although different interrogation methods have been proposed for FBG based sensors, higher resolution and faster detecting speed are always desired in practical applications. Especially for biomedical and soft robotic applications, real-time sensing is necessary for monitoring the deformation or movement during operation. In the future work, a low-cost and real-time interrogation technique for FBG based sensors is expected.

REFERENCES

1. Kersey, Alan D., Michael A. Davis, Heather J. Patrick, Michel LeBlanc, K. P. Koo, C. G. Askins, M. A. Putnam, and E. Joseph Friebele. "Fiber grating sensors." Journal of lightwave technology 15, no. 8 (1997): 1442-1463.
2. Pospíšilová, Marie, Gabriela Kuncová, and Josef Trögl. "Fiber-optic chemical sensors and fiber-optic bio-sensors." Sensors 15.10 (2015): 25208-25259.
3. Wlodarczyk, Marek T., Luciano Coletta, James A. Campbell, and Douglas G. Tomasko. "Fiber optic sensors." U.S. Patent 4,924,870, issued May 15, 1990.
4. Udd, Eric, Ronald J. Michal, Steven F. Watanabe, John P. Theriault, and Richard F. Cahill. "Fiber optic sensor." U.S. Patent 4,787,741, issued November 29, 1988.
5. Schultz, Roger L., Neal Gregory Skinner, Harry Davis Smith Jr, and Daniel David Gleitman. "Fiber optic sensor." U.S. Patent 7,511,823, issued March 31, 2009.
6. Xu, Li, Matthew I. Miller, Jia Ge, Kent R. Nilsson, Zion Tsz Ho Tse, and Mable P. Fok. "Temperature-insensitive fiber-optic contact force sensor for steerable catheters." IEEE Sensors Journal 16, no. 12 (2016): 4771-4775.
7. Ge, Jia, Hanlin Feng, Yue Chen, Zion Tse Ho Tse, and Mable P. Fok. "Spiral-structured fiber Bragg grating for contact force sensing through direct power measurement." Optics express 22, no. 9 (2014): 10439-10445.
8. L. Xu, J. Ge, J. H. Patel, and M. P. Fok, “3-Dimensional Soft Shape Sensor based on Dual-layer Orthogonal Fiber Bragg Grating Mesh,” Optical Fiber Communications Conference (OFC), Th3H.2 (2017).
9. Ge, Jia, Aneek Enrique James, Li Xu, Yue Chen, Ka-Wai Kwok, and Mable P. Fok. "Bidirectional Soft Silicone Curvature Sensor Based on Off-Centered Embedded Fiber Bragg Grating." IEEE Photonics Technology Letters 28, no. 20 (2016): 2237-2240.

10. Chen, Jinjie, Bo Liu, and Hao Zhang. "Review of fiber Bragg grating sensor technology." Frontiers of Optoelectronics in China4, no. 2 (2011): 204-212.

11. 18 Hill, Kenneth O., and Gerald Meltz. "Fiber Bragg grating technology fundamentals and overview." Journal of lightwave technology 15.8 (1997): 1263-1276.

12. Fisher, Norman, and Julian Jones. "Fiber bragg grating fabrication method." U.S. Patent 6,832,025, issued December 14, 2004.

13. Lee, Byoungho. "Review of the present status of optical fiber sensors." Optical fiber technology 9, no. 2 (2003): 57-79.

14. Rao, Y-J. "Fiber Bragg grating sensors: principles and applications." In Optical fiber sensor technology, pp. 355-379. Springer US, 1998.

15. Kashyap, Raman. Fiber bragg gratings. Academic press, 2009.

16. Rao, Yun-Jiang. "Recent progress in applications of in-fibre Bragg grating sensors." Optics and lasers in Engineering 31, no. 4 (1999): 297-324.

17. Chan, T.H., Yu, L., Tam, H.Y., Ni, Y.Q., Liu, S.Y., Chung, W.H. and Cheng, L.K., 2006. Fiber Bragg grating sensors for structural health monitoring of Tsing Ma bridge: Background and experimental observation. Engineering structures, 28(5), pp.648-659.

18. Haijun, Wang Yubao Lan. "Study of Fiber Bragg Grating Sensor System Based on Wavelength-Division Multiplexing/Time-Division Multiplexing [J]." Acta Optica Sinica 8 (2010): 008.

19. Othonos, Andreas. "Fiber bragg gratings." Review of scientific instruments 68, no. 12 (1997): 4309-4341.

20. Patrick, H. J., et al. "Hybrid fiber Bragg grating/long period fiber grating sensor for strain/temperature discrimination." IEEE Photonics Technology Letters 8.9 (1996): 1223-1225.

21. Li, Enbang, Xiaolin Wang, and Chao Zhang. "Fiber-optic temperature sensor based on interference of selective higher-order modes." Applied Physics Letters 89.9 (2006): 091119.

22. Totsu, Kentaro, Yoichi Haga, and Masayoshi Esashi. "Ultra-miniature fiber-optic pressure sensor using white light interferometry." Journal of Micromechanics and Microengineering15, no. 1 (2004): 71.

23. Sutapun, Boonsong, Massood Tabib-Azar, and Alex Kazemi. "Pd-coated elastooptic fiber optic Bragg grating sensors for multiplexed hydrogen sensing." Sensors and Actuators B: Chemical 60, no. 1 (1999): 27-34.

24. Berkoff, T. A., and A. D. Kersey. "Experimental demonstration of a fiber Bragg grating accelerometer." IEEE Photonics Technology Letters 8.12 (1996): 1677-1679.

25. Liang, Wei, Yanyi Huang, Yong Xu, Reginald K. Lee, and Amnon Yariv. "Highly sensitive fiber Bragg grating refractive index sensors." Applied physics letters 86, no. 15 (2005): 151122.

26. Moyo, P., J. M. W. Brownjohn, R. Suresh, and S. C. Tjin. "Development of fiber Bragg grating sensors for monitoring civil infrastructure." Engineering structures 27, no. 12 (2005): 1828-1834.

27. Shah, Dipen, Hendrik Lambert, Arne Langenkamp, Yuri Vanenkov, Giovanni Leo, Pascale Gentil-Baron, and Beat Walpoth. "Catheter tip force required for mechanical perforation of porcine cardiac chambers." Europace 13, no. 2 (2010): 277-283.

28. Chen, Yue, Ka-Wai Kwok, Jia Ge, Yang Hu, Mable Fok, Kent Ronald Nilsson, and Zion Tsz Ho Tse. "Augmented reality for improving catheterization in magnetic resonance imaging-guided cardiac electrophysiology therapy." Journal of Medical Devices 8, no. 2 (2014): 020917.

29. Chen, Yue, Jia Ge, Ka-Wai Kwok, Kent Ronald Nilsson, Mable Fok, and T. Tse Zion. "MRI-conditional catheter sensor for contact force and temperature monitoring during cardiac electrophysiological procedures." Journal of Cardiovascular Magnetic Resonance 16, no. S1 (2014): P150.

30. Polygerinos, Panagiotis, Dinusha Zbyszewski, Tobias Schaeffter, Reza Razavi, Lakmal D. Seneviratne, and Kaspar Althoefer. "MRI-compatible fiber-optic force sensors for catheterization procedures." IEEE Sensors Journal 10, no. 10 (2010): 1598-1608.

31. Wade, Scott A., James B. Fallon, Andrew K. Wise, Robert K. Shepherd, Natalie L. James, and Paul R. Stoddart. "Measurement of forces at the tip of a cochlear implant during insertion." IEEE Transactions on Biomedical Engineering 61, no. 4 (2014): 1177-1186.

32. Wolthuis, Roger A., Gordon L. Mitchell, Elric Saaski, James C. Hartl, and Martin A. Afromowitz. "Development of medical pressure and temperature sensors employing optical spectrum modulation." IEEE Transactions on Biomedical Engineering 38, no. 10 (1991): 974-981.

33. K. Totsu, Y. Haga, and M. Esashi. “Ultra-miniature fiber-optic pressure sensor using white light interferometry,” J. Micromech. Microeng., vol. 15, no. 1, Oct. 2004.

34. Polygerinos, Panagiotis, Tobias Schaeffter, Lakmal Seneviratne, and Kaspar Althoefer. "A fibre-optic catheter-tip force sensor with MRI compatibility: A feasibility study." In Engineering in Medicine and Biology Society, 2009. EMBC 2009. Annual International Conference of the IEEE, pp. 1501-1054. IEEE, 2009.

35. Polygerinos, Panagiotis, Asghar Ataollahi, Tobias Schaeffter, Reza Razavi, Lakmal D. Seneviratne, and Kaspar Althoefer. "MRI-compatible intensity-modulated force sensor for cardiac catheterization procedures." IEEE Transactions on biomedical engineering 58, no. 3 (2011): 721-726.

36. Gardeski, Kenneth C., Michael R. Leners, Jesse T. Torbert, and Ralph J. Thomas. "Multi-lumen steerable catheter." U.S. Patent 7,037,290, issued May 2, 2006.

37. Arkwright, John W., Ian D. Underhill, Simon A. Maunder, Neil Blenman, Michal M. Szczesniak, Lukasz Wiklendt, Ian J. Cook, David Z. Lubowski, and Phil G. Dinning. "Design of a high-sensor count fibre optic manometry catheter for in-vivo colonic diagnostics." Optics express 17, no. 25 (2009): 22423-22431.

38. Song, Hoseok, Heechul Kim, Juwon Jeong, and Jungju Lee. "Development of FBG sensor system for force-feedback in minimally invasive robotic surgery." In Sensing Technology (ICST), 2011 Fifth International Conference on, pp. 16-20. IEEE, 2011.

39. Moerman, Kevin M., Andre MJ Sprengers, Aart J. Nederveen, and Ciaran K. Simms. "A novel MRI compatible soft tissue indentor and fibre Bragg grating force sensor." Medical engineering & physics 35, no. 4 (2013): 486-499.

40. Wang, David Hsiao-Chuan, Neil Blenman, Simon Maunder, Vicki Patton, and John Arkwright. "An optical fiber Bragg grating force sensor for monitoring sub-bandage pressure during compression therapy." Optics express 21, no. 17 (2013): 19799-19807.

41. Neuzil, Petr, Vivek Y. Reddy, Josef Kautzner, Jan Petru, Dan Wichterle, Dipen Shah, Hendrik Lambert, Aude Yulzari, Erik Wissner, and Karl-Heinz Kuck. "Electrical reconnection after pulmonary vein isolation is contingent on contact force during initial treatment." Circulation: Arrhythmia and Electrophysiology 6, no. 2 (2013): 327-333.

42. Kautzner, Josef, Petr Neuzil, Hendrik Lambert, Petr Peichl, Jan Petru, Robert Cihak, Jan Skoda et al. "EFFICAS II: optimization of catheter contact force improves outcome of pulmonary vein isolation for paroxysmal atrial fibrillation." EP Europace 17, no. 8 (2015): 1229-1235.

43. Perna, Francesco, E. Kevin Heist, Stephan B. Danik, Conor D. Barrett, Jeremy N. Ruskin, and Moussa Mansour. "Assessment of catheter tip contact force resulting in cardiac perforation in swine atria using force sensing technology." Circulation: Arrhythmia and Electrophysiology 4, no. 2 (2011): 218-224.

44. Song, Jongseob, Hyunsoo Park, Won-Taek Han, Un-Chul Paek, and Youngjoo Chung. "Induction of sinusoidal chirp in fiber Bragg grating and application to optical fiber sensing with intensity measurements." In Optical Fiber Sensors Conference Technical Digest, 2002. Ofs 2002, 15th, pp. 231-234. IEEE, 2002.

45. Guo, Tuan, Qida Zhao, Hao Zhang, Lifang Xue, Guoyu Li, Bo Dong, Bo Liu, Weigang Zhang, Guiyun Kai, and Xiaoyi Dong. "Temperature-insensitive fiber Bragg grating force sensor via a bandwidth modulation and optical-power detection technique." Journal of lightwave technology 24, no. 10 (2006): 3797-3802..

46. Asbeck, Alan T., Stefano MM De Rossi, Ignacio Galiana, Ye Ding, and Conor J. Walsh. "Stronger, smarter, softer: next-generation wearable robots." IEEE Robotics & Automation Magazine 21, no. 4 (2014): 22-33.

47. Majidi, C., R. Kramer, and R. J. Wood. "A non-differential elastomer curvature sensor for softer-than-skin electronics." Smart Materials and Structures 20, no. 10 (2011): 105017.

48. Song, Shuang, Zheng Li, Max Q-H. Meng, Haoyong Yu, and Hongliang Ren. "Real-time shape estimation for wire-driven flexible robots with multiple bending sections based on quadratic Bézier curves." IEEE Sensors Journal 15, no. 11 (2015): 6326-6334.

49. Park, Yong-Lae, Santhi Elayaperumal, Bruce Daniel, Seok Chang Ryu, Mihye Shin, Joan Savall, Richard J. Black, Behzad Moslehi, and Mark R. Cutkosky. "Real-time estimation of 3-D needle shape and deflection for MRI-guided interventions." IEEE/ASME Transactions On Mechatronics 15, no. 6 (2010): 906-915.

50. Asbeck, Alan T., Stefano MM De Rossi, Ignacio Galiana, Ye Ding, and Conor J. Walsh. "Stronger, smarter, softer: next-generation wearable robots." IEEE Robotics & Automation Magazine 21, no. 4 (2014): 22-33.

51. Daud, S. A., N. H. Mahmood, P. L. Leow, R. Sudirman, and MR Abdul Kadir. "Automated sensor rig in detecting shape of an object." Procedia Computer Science 42 (2014): 153-159.

52. Medina, Oded, Amir Shapiro, and Nir Shvalb. "Resistor-Based Shape Sensor for a Spatial Flexible Manifold." IEEE Sensors Journal 17, no. 1 (2017): 46-50.

53. Chen, Hui, Fei Tian, Jingmao Chi, Jiri Kanka, and Henry Du. "Advantage of multi-mode sapphire optical fiber for evanescent-field SERS sensing." Optics letters 39, no. 20 (2014): 5822-5825.

54. Shin, Woojin, Yeung Lak Lee, Bong-Ahn Yu, Young-Chul Noh, and Tae Jung Ahn. "Highly sensitive strain and bending sensor based on in-line fiber Mach–Zehnder interferometer in solid core large mode area photonic crystal fiber." Optics Communications 283, no. 10 (2010): 2097-2101.

55. Monzon-Hernandez, D., A. Martinez-Rios, I. Torres-Gomez, and G. Salceda-Delgado. "Compact optical fiber curvature sensor based on concatenating two tapers." Optics letters 36, no. 22 (2011): 4380-4382.

56. Caucheteur, C., K. Chah, F. Lhomme, M. Blondel, and Patrice Megret. "Simultaneous bend and temperature sensor using tilted FBG." In Proc. SPIE, vol. 5855, pp. 707-710. 2005.

57. Zhou, Wenjun, Yan Zhou, Xinyong Dong, Li-Yang Shao, Jia Cheng, and Jacques Albert. "Fiber-optic curvature sensor based on cladding-mode Bragg grating excited by fiber multimode interferometer." IEEE Photonics Journal 4, no. 3 (2012): 1051-1057.

58. Allsop, Thomas, Ranjeet Bhamber, Glynn Lloyd, Martin R. Miller, Andrew Dixon, David Webb, Juan Diego Ania Castañón, and Ian Bennion. "Respiratory function monitoring using a real-time three-dimensional fiber-optic shaping sensing scheme based upon fiber Bragg gratings." Journal of biomedical optics 17, no. 11 (2012): 117001-117001.

59. Li, Peng, Zhijun Yan, Kaiming Zhou, Lin Zhang, and Jinsong Leng. "Monitoring static shape memory polymers using a fiber Bragg grating as a vector-bending sensor." Optical Engineering 52, no. 1 (2013): 014401-014401.

60. Moore, Jason P., and Matthew D. Rogge. "Shape sensing using multi-core fiber optic cable and parametric curve solutions." Optics express 20, no. 3 (2012): 2967-2973.

61. Feng, Dingyi, Wenjun Zhou, Xueguang Qiao, and Jacques Albert. "Compact optical fiber 3D shape sensor based on a pair of orthogonal tilted fiber Bragg gratings." Scientific reports 5 (2015): 17415..

62. Smooth-On, Inc. Available at: http://www.smooth-on.com/.

63. A. P. Boresi, R. J. Schmidt, and O. M. Sidebottom, “Advanced mechanics of materials,” vol. 5. pp. 6-7, New York: Wiley, 1993.